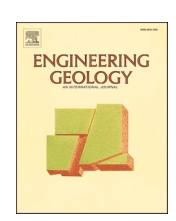
ELSEVIER

Contents lists available at ScienceDirect

## **Engineering Geology**

journal homepage: www.elsevier.com/locate/enggeo





# Experimental study on the stability of noncohesive landslide dams based on seepage effect

Xiao Li a,b, Huayong Chen b,a,b, Xiaoqing Chen b, Tao Wang a,b, Yao Jiang a,b, Hechun Ruan a,b

Abbreviations:  $a_0$ , the height difference between the seepage overflow point and the downstream water level (m);  $a_s$ , the correction factor, taken as 0.0116 (dimensionless); A, the laminar flow coefficient (dimensionless); A<sub>b</sub>, the catchment area (m<sup>2</sup>); b, the bottom width of the breach (m); b, the crest width of the landslide dam measured parallel to the main valley axis (m);  $c_1$ , the correction coefficients, taken as 1.7 (m<sup>0.5</sup>/s);  $c_2$ , the correction coefficients, taken as 1.1 (m<sup>0.5</sup>/s); Cu, the uneven coefficient of dam material (dimensionless); Cu', the uneven coefficient of dam material under seepage influence (dimensionless); Cp, the drag coefficient, which is related to the Reynolds number (dimensionless); C<sub>L</sub>, the drag coefficient, taken as 0.1 (dimensionless); DBI, the dimensionless blockage index (dimensionless); d, the study of soil particle diameter (mm); d<sub>3</sub>, the maximum particle size of the soil for which the soil weight is less than 3 % of the total soil weight in the mass accumulation curve of the soil samples (mm);  $d_{10}$ , the particle size with a cumulative distribution of 10 % (mm);  $d_{10}$ , the particle size with a cumulative distribution of 10 % under seepage influence (mm); d<sub>60</sub>, the particle size with a cumulative distribution of 60 % (mm); d<sub>60</sub>', the particle size with a cumulative distribution of 60 % under seepage influence (mm);  $d_{\text{max}}$ , the maximum particle size of the seepage (mm);  $d_{\text{ski}}$ , the characteristic particle size (mm);  $e_{\text{r}}$ , the soil pore ratio (dimensionless); f, the friction coefficient between the soil particles and the slope (dimensionless); F<sub>f</sub>, the friction between the soil particles and the slope surface (kN);  $F_B$ , the difference between the gravity and buoyancy of the particles,  $F_B = \pi(\rho_s - \rho_w)gd^3/6$  (kN);  $F_C$ , the bonding force between the eroded particles and the slope,  $F_C = \pi \varepsilon (\rho_0/\rho_s)^{2.5} \rho_1 d/2$  (kN);  $F_D$ , the drag force exerted by the water flow,  $F_D = \pi C_D \rho_s u_0^2 d^2/8$  (kN);  $F_P$ , the penetration force,  $F_P = \pi \rho_w g i d^3 (1+e)/6$  (kN);  $F_R$ , the lifting force resulting from the flow velocity differences,  $F_R = \pi C_L \rho_S u_0^2 d^2/8$  (kN);  $h_f$ , the water depth at the breach in the prototype dam (m);  $H_1$ , the water depth at the breach in the model dam,  $H_1 = H_w - H_b$  (m);  $H_2$ , the downstream water level (m);  $H_b$ , the height of the breach (m);  $H_c$ , the non dimensional quantities considering the influence of  $H_d$  and  $Q_s$  (dimensionless);  $H_d$ , the dam height (m);  $H_{dini}$ , the initial dam height (m);  $H_f$ , the flume height (m);  $H_w$ , the upstream water level(m);  $H_w(T)$ , the upstream water level at time T (m); i, the hydraulic gradient (dimensionless);  $i_0$ , the hydraulic gradient of through seepage channels (dimensionless);  $k_s$ , the seepage coefficient of the saturated soil (m/s);  $k_{sm}$ , the tail water submergence correction coefficient, which is set to 1.0 before  $(H_2 - H_b)/(H_w - H_b) \ge 0.67$ (dimensionless);  $k_{\rm D}$  the diversion of inflow rate (dimensionless);  $k_{\rm T}$ , the diversion rate of inflow at time T (dimensionless);  $k_{\rm h}$ , the settlement rate of dam height (dimensionless);  $K_{hT}$ , the settlement rate of dam height at time T (dimensionless); L, the projection of the internal infiltration line of the dam onto the horizontal plane (m);  $L_{\rm f}$ , the flume length (m);  $L_{\rm s}$ , the generalized path of seepage (m);  $L_{\rm u}$ , the distance from the upstream dam site to the flume;  $m_0$ , the coefficient of the breach slope (dimensionless);  $m_1$ , the upstream slope coefficient (dimensionless);  $m_2$ , the downstream slope coefficient (dimensionless);  $p_w$ , the pore water pressure (kPa); q, the average seepage flow rate at the water storage stage (m³/s); Q<sub>b</sub>, the overflow rate (m³/s); Q<sub>r</sub>, the average upstream inflow rate under seepage influence at the water storage stage(m³/s); Q<sub>s</sub>, the upstream inflow rate (m³/s); R<sub>ski</sub>, the ratio of soil loss (dimensionless); i<sub>0</sub>, the initial hydraulic gradient (dimensionless); Δs, The equivalent rectangular width (m); S, the non dimensional parameters considering the geometry characteristics of the dam (dimensionless); S<sub>1</sub>, the change rate of infiltration area at this moment and the previous one ( $m^2/s$ );  $S_s$ , the local longitudinal slope of the channel bed (dimensionless);  $S_{sr}(T)$ , the infiltration area at time T(s); to, the 1 h per unit time (h); Tr, the dimensionless parameter that considers the dam height and upstream inflow rate (dimensionless); Tu, the time scale, taken as 1 (h);  $u_0$ , the viscosity of the breach flow in the prototype dam (m/s);  $u_0$ , the viscosity of the water flowing through the particles (m/s);  $U_0$ , the total mass of lossable soil in 1 kg of soil (kg);  $U_{t,s}^{t}$ , the cumulative loss of the particle mass (kg);  $V_{t,s}^{t}$ , the landslide dam volume (m<sup>3</sup>);  $V_{t,s}^{t}$ , the volume of water ponded behind the dam (m<sup>3</sup>);  $V_{t,s}^{t}$ , the real volume of water ponded behind the dam in this study ( $m^3$ );  $W_d$ , the base width of the landslide dam measured parallel to the main valley axis (m);  $W_b$ , the flume width (m);  $W_1$ , the length of the water tank (m);  $W_2$ , the width of the water tank (m); y, the dimensionless quantities that characterize stability, y > 0 unstable, y < 00 stable (dimensionless); a, the overall angle between the downstream slope and the dam foundation (°); a, the angle between the seepage force and horizontal plane (°);  $\alpha_{sm}$  the shape coefficient, typically ranging from 1.16 to 1.17 (dimensionless);  $\beta$ , the overall angle between the dam foundation and the horizontal plane (°);  $\gamma_{ws}$ the unit weight of water  $(kN/m^3)$ ;  $\varepsilon$ , the bonding force parameter (dimensionless);  $\theta_1$ , the angle between the cohesion and horizontal plane  $(\circ)$ ;  $\theta_2$ , the angle between the composite flow force and downstream slope (°);  $\theta_3$ , the angle between the friction force of the starting particles and the slope surface (°);  $\lambda_1$ , the dimensionless coefficient,  $\lambda_1 = f \cos \alpha - \sin \alpha$  (dimensionless);  $\lambda_2$ , the dimensionless coefficient,  $\lambda_2 = \cos (\alpha - \theta_2) + f \sin (\alpha - \theta_2)$  (dimensionless);  $\lambda_3$ , the dimensionless coefficient,  $\lambda_3 = \cos{(\alpha + \theta_1)} - f\sin{(\alpha + \theta_1)}$  (dimensionless);  $\lambda_4$ , the dimensionless coefficient,  $\lambda_4 = \sin{\theta_3}$  (dimensionless);  $\lambda_5$ , the dimensionless coefficient,  $\lambda_5 = \cos{(\alpha - \theta_2 + \theta_3)}$ (dimensionless);  $\lambda_6$ , the dimensionless coefficient,  $\lambda_6 = \cos(\theta_3 + \theta_1)$  (dimensionless);  $\rho_0$ , the dry density of soil particles (kg/m<sup>3</sup>);  $\rho_1$ , the fluid density (kg/m<sup>3</sup>);  $\rho_5$ , the density of soil particles (kg/m<sup>3</sup>);  $\rho_{\rm w}$ , the density of water (kg/m<sup>3</sup>)...

\* Corresponding author at: Key Laboratory of Mountain Hazards and Surface Process, CAS/ Institute of Mountain Hazards and Environment, CAS, Chengdu 610299, China.

E-mail address: hychen@imde.ac.cn (H. Chen).

https://doi.org/10.1016/j.enggeo.2024.107708

a Key Laboratory of Mountain Hazards and Earth Surface Process, CAS/ Institute of Mountain Hazards and Environment, CAS, Chengdu 610299, China

<sup>&</sup>lt;sup>b</sup> University of Chinese Academy of Sciences, Beijing 100049, China

#### ARTICLE INFO

Keywords:
Seepage
Noncohesive landslide dam
Dam stability
Experiments
Dam characteristics

#### ABSTRACT

Landslide dams composed of unconsolidated, noncohesive soil are easily affected by seepage. As seepage develops, the dam's characteristics change dynamically, indirectly affecting its stability. However, previous studies on dam failure have mostly assumed that the dam characteristics remain constant before failure, often overlooking these changes and their effects on stability. In this study, 48 sets of flume experiments were conducted to quantify the impact of seepage under varying upstream inflow rates, dam heights, downstream slope angles, and particle size distributions. During the storage phase, the rise rate of the water level is closely linked to the seepage's diversion capacity. The diversion rate of inflow reached as high as 0.747 in this study, but decreased to 0.230 as inflow increased. Furthermore, changes in the internal stress distribution within the dam, driven by seepage, contributed to dam settlement and the sliding of the downstream slope. Notably, dam settlement exhibited both non-uniform spatial distribution and temporal stage development. The maximum settlement ratio between the point in the upstream breach and the point in the downstream breach reached as high as 2.79. Regarding the soil changes within the dam, after the seepage channel became connected, the primary soil loss involved silt particles ranging from 10 to 20 µm in size. This result reflects the increasing non-uniformity within the dam caused by seepage. Finally, Considering the changes in dam characteristics under the influence of seepage, in this study, a logistic regression model was established to assess dam stability. Overall, this study enhances the understanding of how seepage affects dam stability by examining various dam properties and presenting a model for stability assessment.

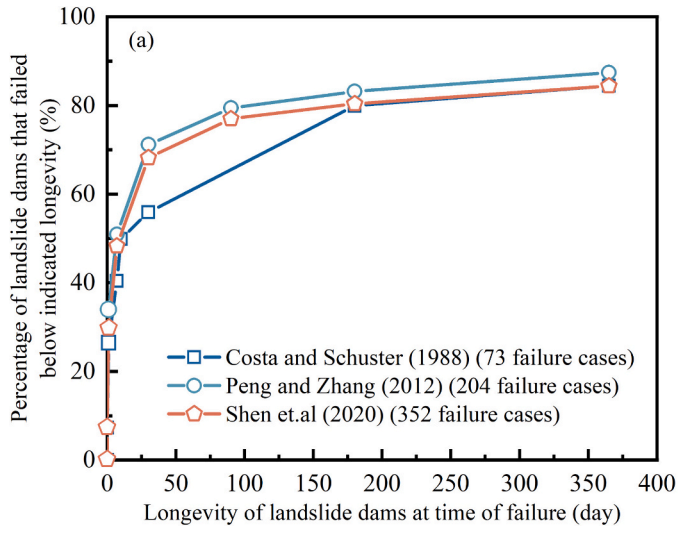
#### 1. Introduction

In recent years, there has been a significant increase in extreme geological disasters, characterized by frequent rainstorms and earth-quakes, which have triggered numerous landslides that block rivers (Costa and Schuster, 1988; Korup, 2004; Zheng et al., 2021). Landslide dams, which form naturally and obstruct rivers, are typically composed of loose materials, exhibit uneven particle distribution, and vary in external shape. Due to the lack of artificial anti-seepage measures, such as geomembranes and cutoff walls, for dams made of cohesionless materials, seepage can easily compromise their stability, especially when there is a large difference in water head between the upstream and downstream (Chen et al., 2021a; Jiang et al., 2019; Nian et al., 2020; Shen et al., 2020; Zheng et al., 2021; Shen et al., 2022; Shi et al., 2022; Nardini et al., 2024). Therefore, systematically analyzing dam stability with respect to seepage provides valuable insights for mitigating the hazards posed by noncohesive landslide dams.

Due to the sudden nature of landslide dams, fitting formulas based on past cases are often used for the rapid assessment of dam stability. Considering the influence of upstream catchment conditions and dam geometric characteristics, Canuti et al. (1998) proposed the blockage index ( $BI = \log{(V_{\rm d}A_{\rm b}^{-1})}$  to assess dam stability (Swanson et al., 1986).

Furthermore, Ermini and Casagli (2003) introduced the dimensionless blockage index ( $DBI = \log{(A_bH_dV_d^{-1})}$ ), which emphasizes the influence of dam height in overtopping failures. Similarly, Dong et al. (2011b) developed logistic models for dam stability taking into account various geomorphic variables. In addition, Stefanelli et al. (2016) presented a hydromorphological dam stability index ( $HDSI = \log{(V_lA_b^{-1}S_l^{-1})}$ ), which considers dam destabilization due to river flow using a simplified expression of stream power per unit channel length. Liao et al. (2022) established a graded evaluation system for dam stability based on indicators such as geometric parameters, material composition, longevity, and spillway characteristics. Zheng et al. (2021) provided a qualitative analysis of overtopping and seepage failures based on a study of 1737 worldwide cases. These studies have developed several statistical formulas for assessing the stability of barrier dams, yet they have rarely accounted for specific dam failure mechanisms.

In fact, approximately one-third of landslide dams last less than one day, and half last less than one week (Fig. 1). This short longevity makes it difficult to observe the complete failure process of the dam (Shen et al., 2020; Zhong et al., 2021). As a result, Zheng et al. (2024) suggested that the small-scale dam tests can be used to study the failure processes and mechanisms of landslide dams. Based on model dam experiments, the failure modes of landslide dams and the effects of seepage



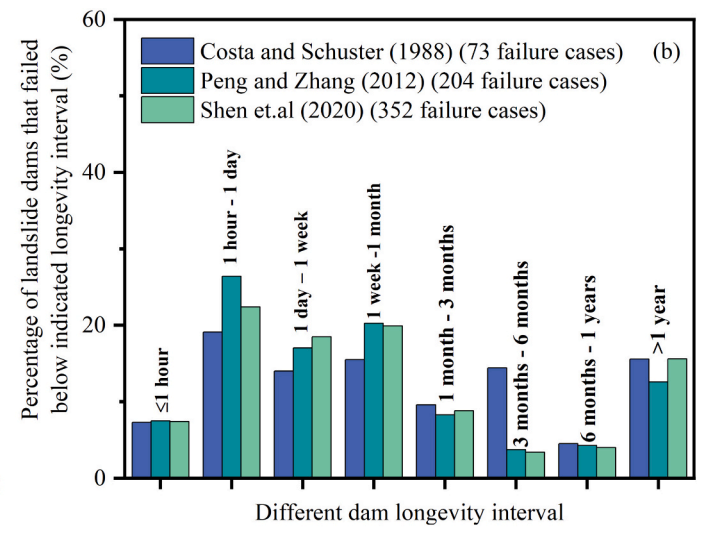
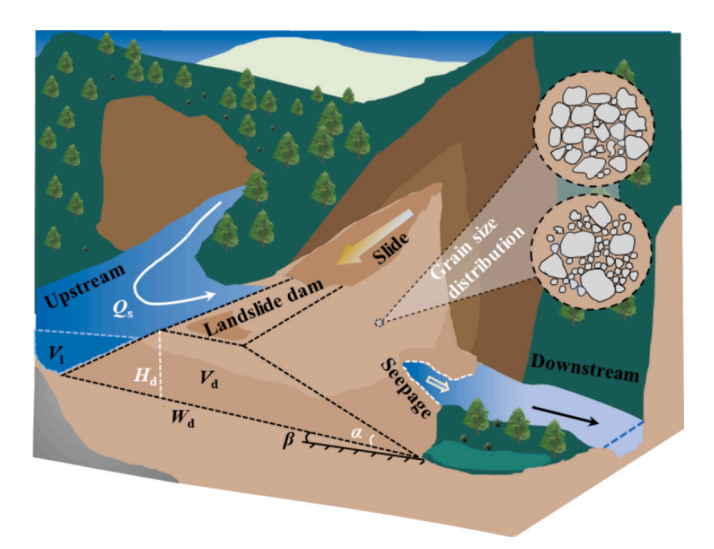


Fig. 1. Statistics of dam longevity (Shen et al., 2020): (a) the longevity of landslide dams at time of failure; (b) different dam longevity interval.



**Fig. 2.** The model parameters considered in this study based on recent literature (Liu et al., 2023; Ruan et al., 2021b; Zhou et al., 2022b) and the detail description of these symbols are shown in the abbreviations. The white symbols in the figure represent the variables selected in this study.

and overflow on downstream slope erosion during dam failures have been investigated in previous studies (Chen et al., 2015; Shrestha and Nakagawa, 2016; Shen et al., 2022; Shi et al., 2022; Zhou et al., 2022a). In the same time, consider the influence of seepage on the dam staibility, Peng et al. (2021) indicated that the breaching duration decrease with the increase of mean particle size. Chen et al. (2023) emphasized the amplification effect of soil material changes due to piping on outburst floods. Shen et al. (2024) suggested that variations in soil distribution within the dam have a controlling effect on the failure process, highlighting the strengthening effect of non-uniform soil distribution. However, most of these studies treat the dam before failure as a static entity, rarely considering the dynamic changes in upstream conditions, external geometry, and internal material distribution throughout the water storage stage. Based on the long-term observational data, Shafieiganjeh et al. (2024) indicated that the displacements in dam crown of a long-existing landslide dam depends on the ratio of the lake level changes, which are related to the effect of force distribution caused by seepage development. Nevertheless, directly applying these mechanism analyses to the rapid assessment of sudden landslide dam stability remains challenging.

In this study, 48 sets of flume experiments were conducted to quantitatively analyze the dynamic alterations in dam characteristics casued by seepage under varying inflow rates, dam heights, downstream slope angles, and particle size distributions during the water storage phase. Simultaneously, the impacts of these changes in dam characteristics were examined by analyzing the equilibrium relationship of soil particle initiation on the slope under the combined effects of seepage and overflow. Based on the quantitative evaluation of changes in dam characteristics, a logistic regression model of dam stability was developed, and its accuracy and applicability were analyzed and verified by six cases. These results can serve as a reference for emergency responses to barrier dam disasters.

#### 2. Materials and methods

## 2.1. Model setup

There are differences between dam models and natural dams. Thereby, Peng and Zhang (2012) introduced several geometric parameters to characterize dam design, including the ratio of dam height to dam width  $(H_{\rm d}/W_{\rm d})$ , the dam shape coefficient  $(V_{\rm d}^{1/3}/H_{\rm d})$ , and the lake coefficient  $(V_{\rm d}^{1/3}/H_{\rm d})$ . These parameters were used to assess the

Table 1

Parameters of this study: the UI group has changed the upstream inflow; the DH group has changed the dam height; the SA group has changed the downstream slope angle; and the GA group has changed the grain size distribution. In this study, the basic parameters were set as follows:  $Q_{\rm S}=0.35\times 10^{-3}~{\rm m}^3/{\rm s}$ ,  $H_{\rm d}=30~{\rm cm}$ ,  $\alpha=25^{\circ}$ , G8(Grain size distribution).

Group	Upstream inflow rate $Q_s$ (×10 <sup>-3</sup> m <sup>3</sup> /s)	Dam height H <sub>d</sub> (cm)	Downstream slope angle $\alpha$ (°)	Grain size distribution
UI DH SA GS	0.20–2.50 0.35 0.35 0.35	30 20–50 30 30	25 25 15–35 25	G8 G8 G1 ~ G10

**Table 2**Grain size distribution design. The initial soil refers to the soil (has been sieved out particles larger than 2 cm) that without percentage adjustment of particle group in this study.

Grain size distribution	Particle content (%)						
	Group 1 (20–10 mm)	Group 2 (<10 mm)					
G1	Initial soil						
G2	0	100					
G3	10	90					
G4	20	80					
G5	30	70					
G6	40	60					
G7	50	50					
G8	60	40					
G9	70	30					
G10	80	20					

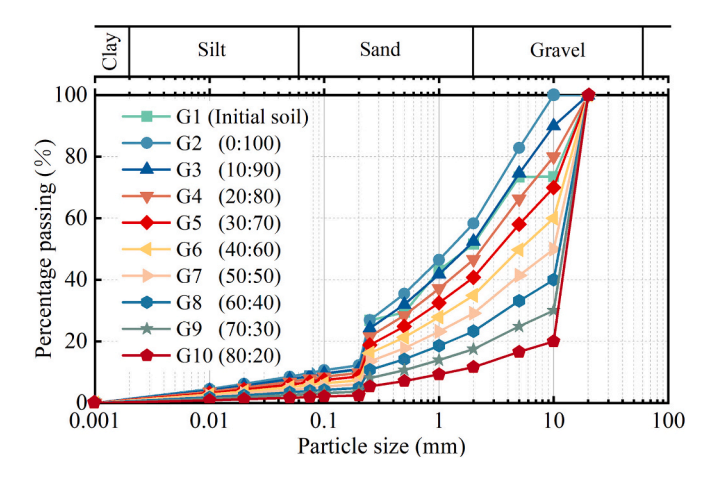


**Fig. 3.** Grain size distribution. The Gn (a:b) refers to Grain size distribution number (percentage of group 1: percentage of group 2), as shown in Table 2.

similarity between model dams and natural dams (Ruan et al., 2021b; Zhou et al., 2022a). In addition, Li et al. (2021) proposed the use of the hydrodynamic coefficient ( $(Q_sT_u)^{1/3}/H_d$ ) as an indicator of the upstream inflow rate ( $Q_s$ ), where  $T_u=1$  s. Furthermore, the Froude number ( $F_r=u_f(gh_t)^{0.5}=u_o(gH_1)^{0.5}$ ) can be used to characterize the similarity of flow fields between the model and prototype dams under gravity (Shen, 2022).

The failure process of noncohesive landslide dams is governed by complex interactions (Fig. 2) among hydrological parameters (such as upstream inflow rate and lake volume), dam geometry, and dam material properties (Zheng et al., 2021; Macchione and Graziano, 2024). Given the significant variability in the size and geometric characteristics of landslide dams in the field, this study did not focus on a specific dam as a case study but instead aimed to investigate the impact of seepage on non-cohesive landslide dams more generally. Based on previous studies

**Table 3**Range of five characteristic parameters of model.

	$H_{\rm d}/W_{\rm d}$	$V_{\rm d}^{1/3}/H_{\rm d}$	$V_{\rm l}^{1/3}/H_{\rm d}$	$(Q_{\rm s}T_{\rm u})^{1/3}/H_{\rm d}$	$F_r$
Cases	0.030-1.000	1.000-30.000	1.000-31.000	0.007-2.429	0.300-3.500
This study	0.148-0.371	1.107-21.892	1.648-8.396	0.002-2.500	0.357-3.371

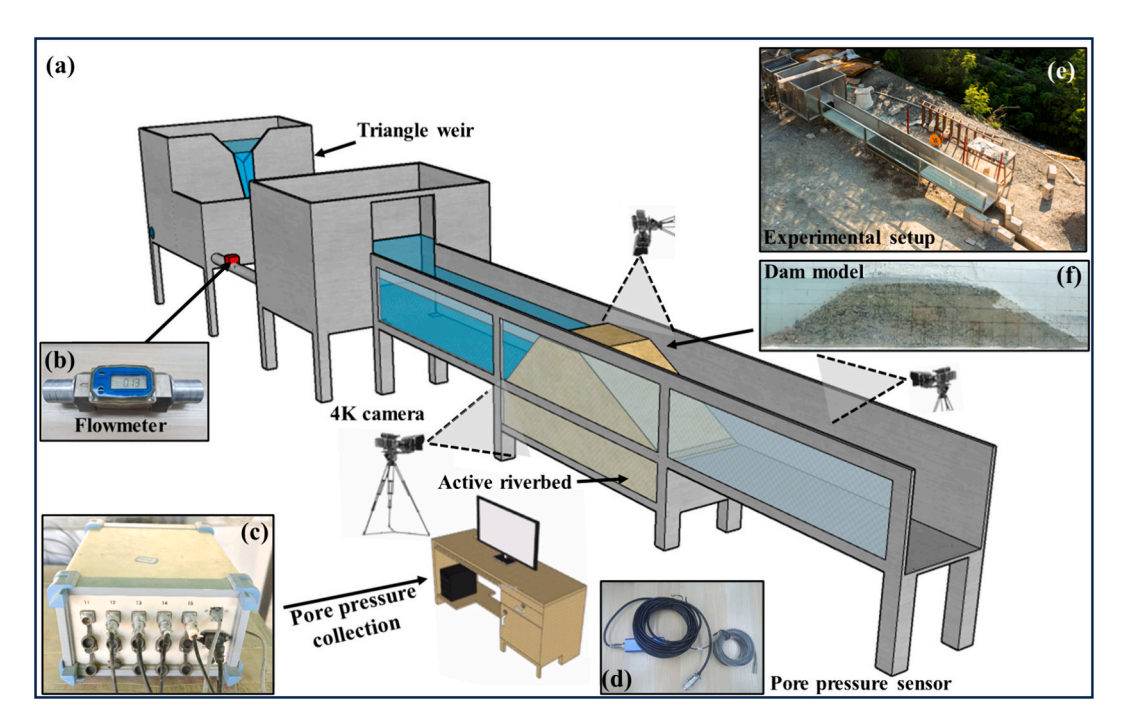


Fig. 4. Experimental: (a) experimental setup model; (b) flowmeter; (c) pore pressure collection; (d) pore pressure sensor; (e) physical setup of the experimental; and (f) dam model.

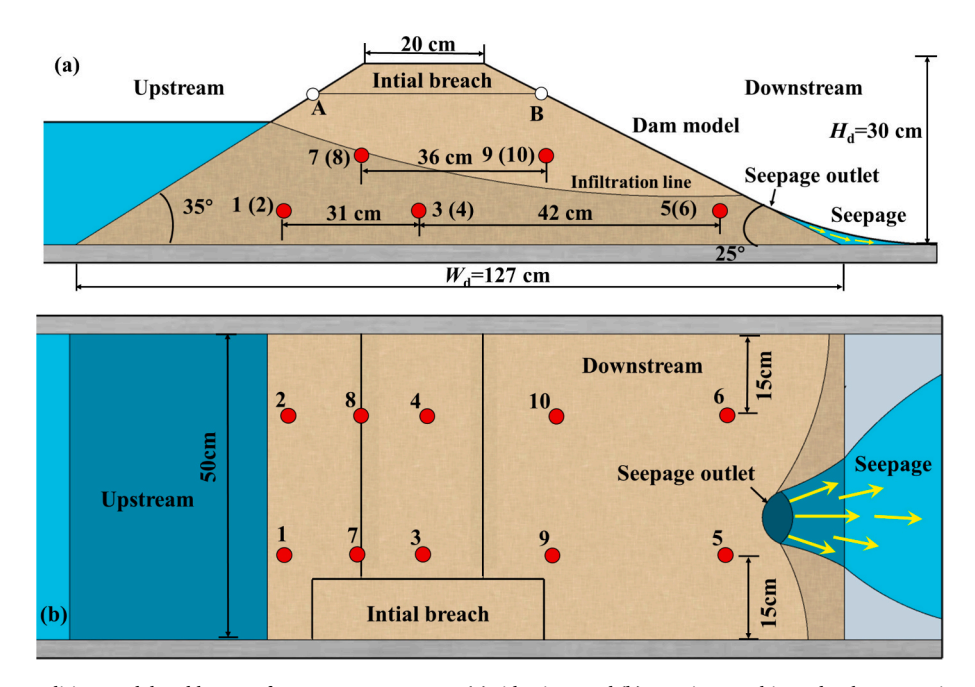
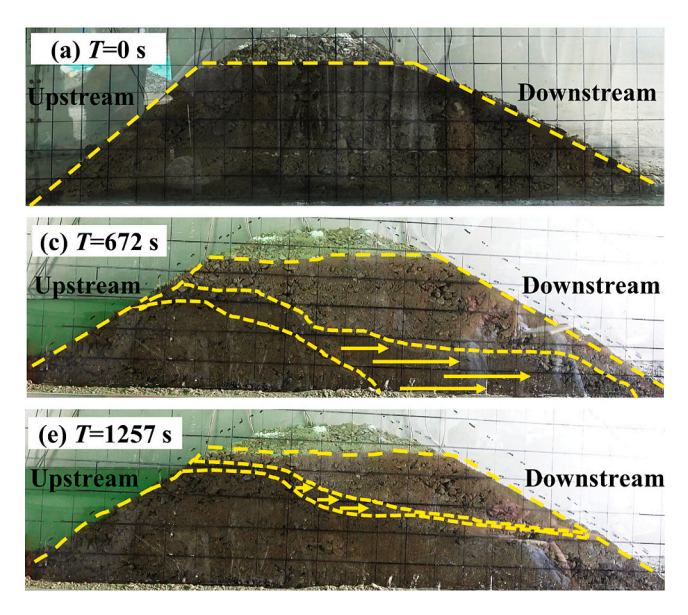
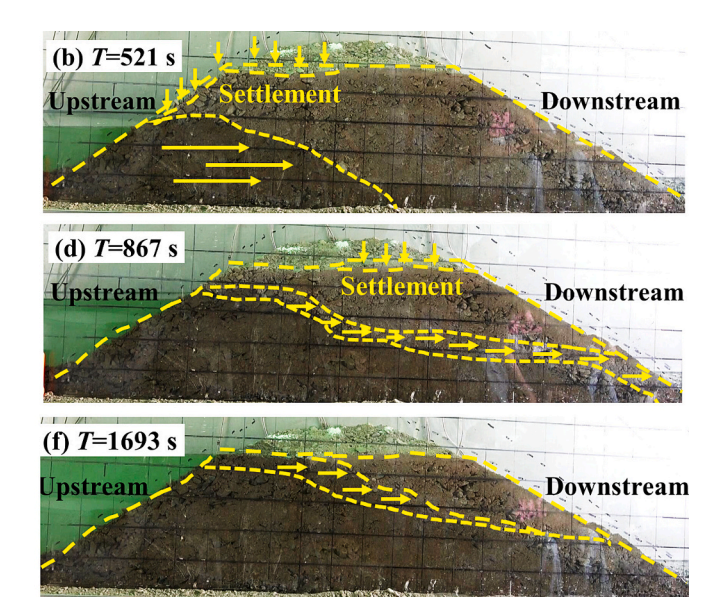


Fig. 5. Standard working condition model and layout of pore pressure sensors: (a) side view; and (b) top view. In this study, the reservoir capacity of the dam ranged from 0.20 to 0.53 m<sup>3</sup>.

(Jiang et al., 2020; Ruan et al., 2021a; Shi et al., 2015; Zhou et al., 2022a; Zheng et al., 2024), this study selected four key variables: upstream inflow rate (UI), dam height (DH), downstream slope angle (SA)

and grain size distribution (GS) (Table 1). Different grain size distributions were selected by changing the proportions of group 1 (20–10 mm) and group 2 (less than 10 mm) (Table 2 and Fig. 3). A comparison of





**Fig. 6.** Seepage development process. (a) T=0 s, the moment when the upstream reaches the upstream slope foot of the dam; (b) T=521 s, the water level reached 12.5 cm, and at the same time, settlement occurred in the upstream dam body; (c) T=672 s, the infiltration line reaches to the foot of the downstream dam slope; (d) T=867 s, settlement occurred in the downstream dam body; (e) T=1257 s, the seepage appears on the downstream slope surface; (f) T=1693 s, the water level reaches the initial breach.

similarity between the model dam and the prototype dam is shown in Table 3.

#### 2.2. Experimental setup

The experimental setup was conducted at the Dongchuan Debris Flow Observation Station (DDFOS) and comprised a triangular weir, a storage reservoir, and a main flume (Fig. 4). To measure the inflow, the triangular weir was paired with an electronic flowmeter for verification. A storage reservoir, with dimensions of 1.0 m  $\times$  0.5 m  $\times$  0.5 m, provided the primary storage capacity for the model. Measuring 6.0 m  $\times$  0.5 m  $\times$  $0.5 \text{ m} (L_f \times W_f \times H_f)$ , the main flume featured an adjustable longitudinal slope. To minimize the impact of the smooth bottom plate on seepage dynamics, a 20 cm thick soil layer was placed in the central section of the flume, simulating a natural riverbed. During the experiment, a digital high-definition camera (24 frames per second) was used to meticulously document the intricate process of seepage development within the dam. To thoroughly assess the pore pressure dynamics inside the dam, two horizontal planes were equipped with DY202 pore water pressure sensors, with an accuracy of 0.1 % and a range of  $\pm 20$  kPa. The configuration of the additional sensors is illustrated in Fig. 5.

#### 2.3. Experiment procedure

The detailed experimental procedure is as follows:

- (1) Flume preparation: The dam contours were drawn on the side-wall of the flume based on the predesigned dam shape. Then the water pump was powered on, and the flow rate was adjusted to the experimental design value using the triangular weir and flowmeter. Group 1 and Group 2 materials were mixed in different proportions according to the grain size distribution shown in Fig. 3 to prepare the dam models.
- (2) Dam Construction: The water pump was turned off, and the dam model was constructed naturally, followed by manual trimming as needed. Pore pressure sensors were installed during the dam construction process. An initial breach was excavated on the right side of the dam crest with dimensions of 5 cm in height and 10 cm in width.

- (3) Flume Experiment Process: Once dam construction was complete, all instruments were activated simultaneously (Fig. 4). The water valve was opened to allow inflow into the dammed lake. Observations were made in the downstream flume, and when turbid water flows became visible, 100 ml of fluid was sampled every 300 s. During this process, the stability of the data curve from the water level sensor in front of the dam was monitored, which allowed for determining the conclusion of the dam failure process.
- (4) Geotechnical Experiment Process: After the flume experiments, the turbid flow was dried to obtain the seepage soil, and the particle size distribution of the soil was measured using the Marvin experiment. Additionally, the permeability coefficients of six dam materials were determined based on permeability experiments.
- (5) Data Processing: Pore pressure data were obtained from the pore pressure sensors, while dam stability and water levels were assessed from recorded video. The effective inflow rate  $Q_{\rm r}$  can be calculated from the water level upstream of the dam:

$$Q_{\rm r} = \frac{V(T + \Delta T) - V(T)}{\Delta T} \tag{1}$$

The diversion rate  $(k_{rT})$  of inflow at time T as calculated:

$$k_{\rm rT} = 1 - \frac{V(T + \Delta T) - V(T)}{Q_{\rm s} \Delta T} \tag{2}$$

At time T, the volume of the reservoir is calculated according to storage relationship:

$$V(T) = W_1 \times W_w \times H_w(T) + \frac{1}{2}H_w(T) \times \left[2L_u + H_w(T)\cot(\beta)\right] \times W_f$$
 (3)

The development of the infiltration area could be calculated

$$S_{s} = \frac{S_{\rm sr}(T+\Delta T) - S_{\rm sr}(T)}{\Delta T} \tag{4} \label{eq:ss}$$

The settlement rate ( $k_{\rm hT}$ ) at time T was calculated from the dam height:

$$k_{\rm hT} = \frac{H_{\rm d}(T + \Delta T) - H_{\rm d}(T)}{H_{\rm dini}} \tag{5}$$

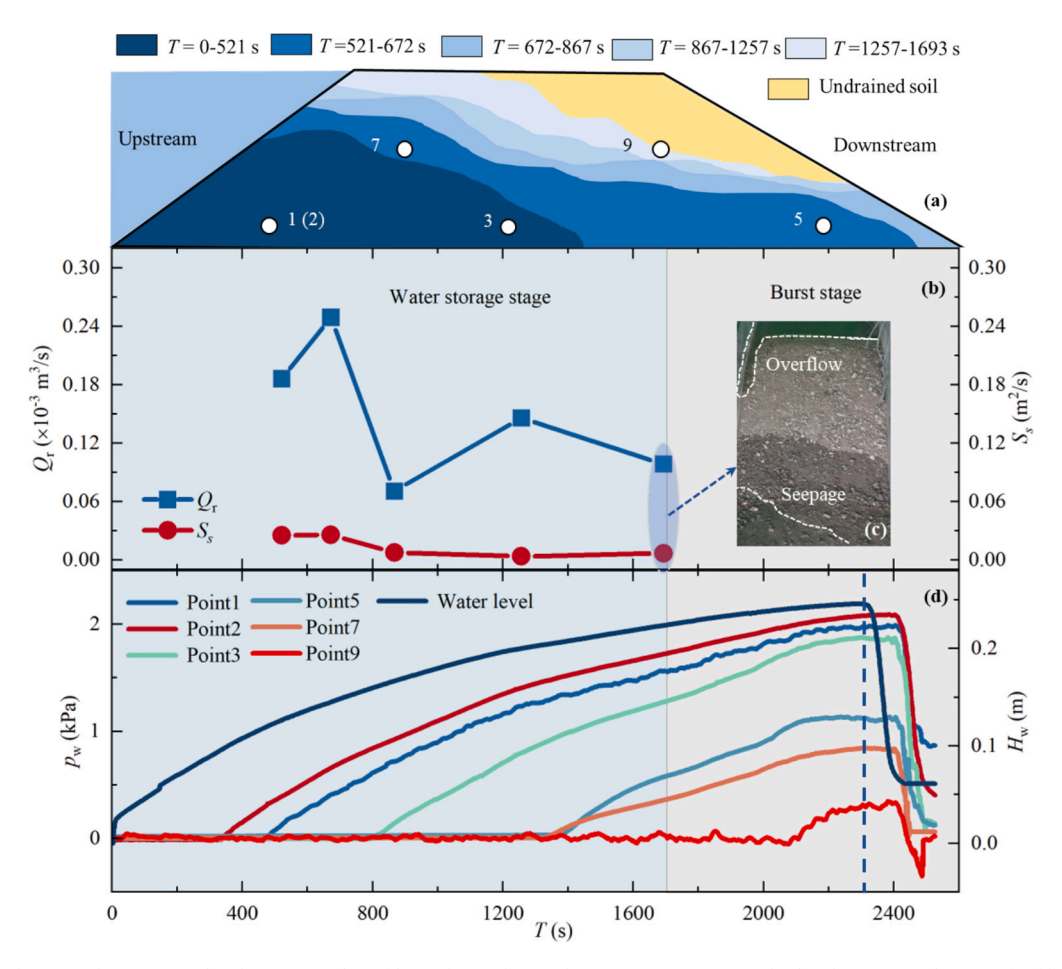


Fig. 7. Seepage development diagram: (a) development to the infiltrated area during the water storage stage; (b) development to the rate of infiltration area and rate of change of the water volume in front of the dam during the water storage stage; (c) the end of the water storage; and (d) pressure comparison of the pore pressure inside the dam.

## 3. Experimental results

## 3.1. Overall development characteristics of seepage

To reflect the seepage process, we introduce the case of GS1 ( $Q_s =$  $0.35 \times 10^{-3}$  m<sup>3</sup>/s,  $H_d = 30$  cm,  $\alpha = 25^{\circ}$ , and grain size distribution 1). According to previous studies (Ruan et al., 2021b; Shen et al., 2022; Zhou et al., 2022a), the dam failure process can be divided into two stages: the water storage stage and the burst stage. T = 0 s marks the beginning of the water storage stage when the inflow reaches the foot of the upstream slope (Fig. 6 a). At T = 0-521 s, variations in pore pressure occur at different locations along the river due to seepage, caused by the water head difference. These variations in pore pressure lead to changes in the internal stress distribution within the dam, resulting in differential settlement along various sections of the river (ranging from 0.5 cm to 3 cm) (Fig. 6 b). At T = 521-672 s (Fig. 6 c, Fig. 7 a, b), considering the correlation between the development rate of the infiltration area and the seepage rate (Meng et al., 2021), the macroscopic effect of increased seepage, driven by the rising head difference, is reflected in an accelerated rate of infiltration area expansion. Meanwhile, settlement occurs in the rear section of the dam, ranging from 2 to 2.5 cm (Fig. 6 d). At T =673-867 s, the rates of water volume change and infiltration area development within the dam begin to slow (Fig. 7 c, d). At T =1257–1693 s, the rise in water level slows further (Fig. 6 e, f). At T >1693 s, the water level rises to the initial breach, and the upstream water storage begins to overflow (Fig. 6 f). This marks the end of the water storage stage and the beginning of the burst stage. At this point, the upstream water volume is influenced not only by inflow and seepage but also by overflow (Fig.  $7\,$  c).

A direct correlation between variations in the pore water pressure and the failure process can ehance the understanding of the failure mechanism. During the process of seepage development, as can be seen from Fig. 7 d the order of the change in the pore pressure inside the dam is 1–3–5-7-9 during the water storage stage.

During the burst stage, notably, the peak pore water pressures at No.1 (1.987 kPa) and No.3 (1.835 kPa) are 1.625 to 1.760 times higher than that at No.5 (1.129 kPa). The variation of pore pressure can to some extent reflect the internal stress changes of the dam (Zhou et al., 2022a). The pore pressure peak in the upstream measuring point exceeds the downstream one(Fig. 7 d), indicating a diminishing impact of seepage on the internal stress of the soil in the downstream direction. Due to the erosion of the traceability scarp on the right side of the dam, the sensor at the downstream measuring point No.5 was the first to be affected by the overflow, resulting in an earlier sudden drop in the pore pressure compared with those at points No. 1 and No. 3.

Horizontally, as shown in Fig. 7 d, the peak pore pressure at point No. 1 is higher than that at point No. 2, and the change at point No. 1 occurs earlier. This indicates that seepage within the dam develops in a three-dimensional space rather than linearly. At  $T=2321\,$  s, after the water level begins to drop, pore pressure initially experiences a short period of increase before eventually decreasing. This behavior suggests a 120 s lag in the dam's pore pressure response to changes in the water level. Simultaneously, as overflow erosion intensifies on the dam, the pore pressure inside the dam sharply decreases.

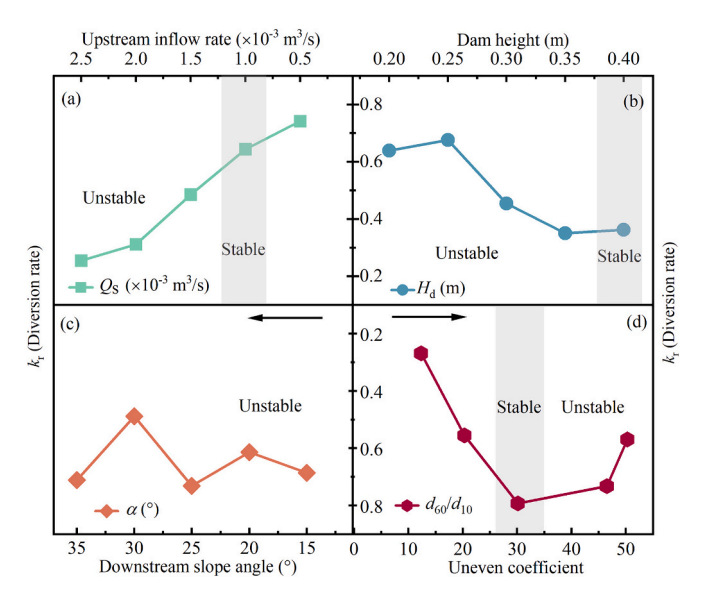


**Fig. 8.** Influences of various factors on diversion rate: (a) the influence of inflow rate; (b) the influence of dam height; (c) the influence of slope angle; (d) the influence of uneven coefficient.

## 3.2. Diversion of inflow

Water infiltration and downstream slope outflow reduce the effective inflow, which directly affects the growth rate of the water head during the water storage stage (Casagli and Ermini, 1999; Ming et al., 2022; Shi et al., 2022). The diversion rate  $k_{\rm r}$  induced by dam seepage can be defined as the ratio of the average seepage flow ( $q=Q_{\rm s}-Q_{\rm r}$ ) during the water storage stage to the theoretical upstream inflow rate. In this study, the diversion rate was 31.1–74.3 %.

As the inflow rate increases, the diversion rate decreases correspondingly (Fig. 8 a), which may due to there is a significant threshold for the discharge capacity of the soil section within a specific time unit. Additionally, the diversion rate decreases with increasing initial height of dam (Fig. 8 b). When  $H_d$  reaches 0.40 m, the landslide dam exhibits stability. This demonstrates that, although seepage influence may be higher in lower dams at the same water level, once H<sub>d</sub> falls below a certain threshold, the risk of overtopping increases significantly due to the smaller storage capacity. As the downstream slope angle decreases, the diversion rate shows an overall declining trend, fluctuating between 0.48 and 0.73 (Fig. 8 c). Referring to Fig. 8 d, the diversion rate of seepage in the dam initially increases, followed by a decline as the uneven distribution rate increases. In this study, when the uneven distribution rate reaches 30.11, the soil skeleton within the dam transitions from a coarse particle structure to a fine particle structure. Comparatively, the fine particle skeleton is more prone to collapse and blockage than the coarse particle skeleton, thereby hindering the formation of dominant seepage channels in the dam.

Based on 48 sets of model experiments, 34 sets of data were randomly selected to establish the relationship between  $k_{\rm r}$ , dam height  $H_{\rm d}$ , upstream inflow rate  $Q_{\rm s}$ , uneven coefficient  $d_{\rm 60}/d_{\rm 10}$ , downstream slope angle  $\alpha$ , dam width  $W_{\rm d}$  and gravitional acceleration g:

$$k_{\rm r} = f(H_{\rm d}, Q_{\rm s}, d_{60}/d_{10}, \tan\alpha, W_{\rm d}, g)$$
 (6)

Using  $Q_s$  and g as the basic dimensionless quantities to measure variables, we can obtain

$$k_{\rm r} = f\left(\frac{H_{\rm d}}{\sqrt[5]{Q_{\rm s}^2/g}}, \frac{d_{60}}{d_{10}}, \tan\alpha, \frac{W_{\rm d}}{H_{\rm d}}\right) \tag{7}$$

 $H_{\rm c}=H_{\rm d}/(Q_{\rm s}^2/g)^{0.2}.$  Based on the data obtained, further fitting can be conducted to obtain:

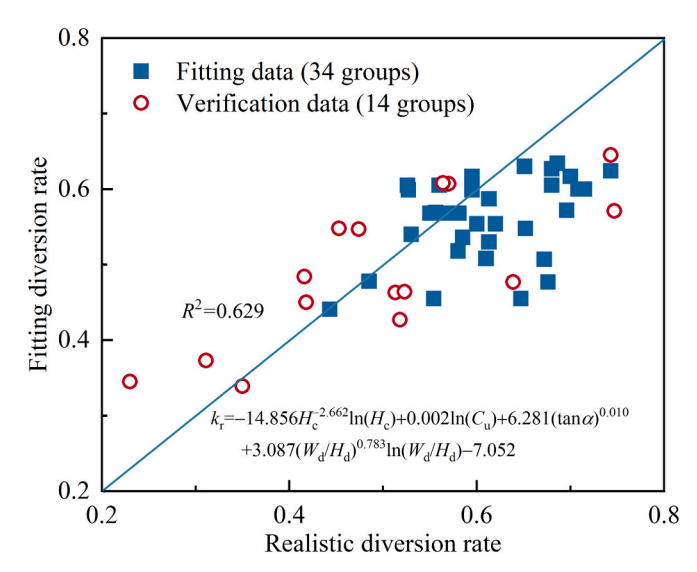
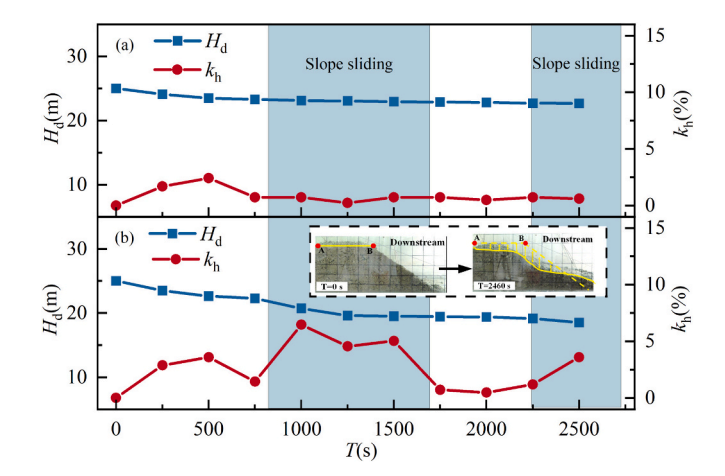


Fig. 9. Verification of prediction formula of diversion rate.



**Fig. 10.** Changes in the dam height and settlement: (a) point A; and (b) point B. The settlement rate of the dam  $(k_h)$ , defined as the ratio of the height difference  $(\Delta H_d)$  to the initial height  $(H_d)$  within a certain time period  $(\Delta T)$  in a unit length range.

$$\begin{split} k_{\rm r} &= -\frac{14.856 ln(H_{\rm c})}{H_{\rm c}^{2.662}} + 0.002 C_{\rm u}^{0.339} ln(C_{\rm u}) + 6.281 (tan\alpha)^{0.010} \\ &+ 3.087 \frac{H_{\rm d}^{0.783}}{W_{\rm d}^{0.783}} ln\bigg(\frac{W_{\rm d}}{H_{\rm d}}\bigg) - 7.052 \end{split} \tag{8}$$

 $R^2$  of the fitted Eq. (8) determined using 34 randomly selected datasets was calculated to be 0.629. Given the limited existing research and data discussion about this particular issue, the formula was further validated using the remaining 14 datasets. The verification results are presented in Fig. 9.

## 3.3. Change in dam geometry

Seepage affects the stress distribution within the dam by increasing water content and eroding soil particles (Chen et al., 2023; Liu et al., 2023), which induces settlement and sliding of the downstream slope. To investigate the specific development process, the GS6 ( $Q_{\rm s}=0.35\times10^{-3}~{\rm m}^3/{\rm s}$ ,  $H_{\rm d}=30~{\rm cm}$ ,  $\alpha=25^\circ$ , grain size distribution 6) was selected.

As shown in Fig. 10, at point A, rapid soil settlement occurs between 0–250 s, followed by a slower settlement after 250 s. In contrast, point B experiences three distinct periods of rapid settlement: 0–750 s,

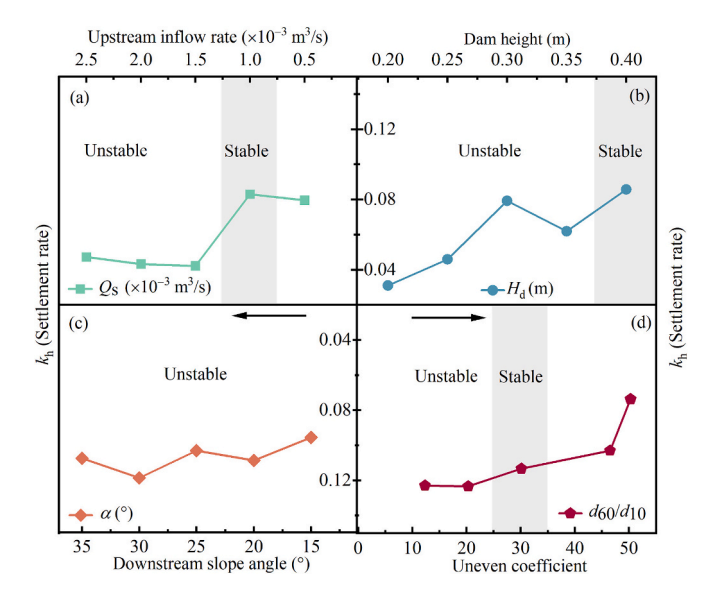


**Fig. 11.** Influences of various factors on settlement rate: (a) the influence of upstream inflow rate; (b) the influence of dam height; (c) the influence of slope angle; (d) the influence of uneven coefficient.

751–1750 s, and 2250–2750 s. Notably, the sharp drops in settlement at point B during the intervals of 750–1750 s and 2250–2750 s are primarily attributed to the sliding of the downstream slope, as indicated by the change in slope inclination from 35.0° to 21.1°(Fig. 10). Consequently, the consolidation settlement of the dam under the influence of seepage can be summarized as exhibiting non-uniform development along the river and phased development over time. Furthermore, the sliding of the slope not only reduces the dam height but also strengthens the erosion resistance of the downstream slope (Liu et al., 2023; Zhang et al., 2023). However, in this experiment, only 12.5 % of the observed cases exhibited significant slope instability, where the ratio of the slope angle before and after the change exceeded 1.2. Consequently, the following analysis primarily focuses on investigating changes in dam height.

The actual settlement rate of the dam can be determined by averaging the settlement rates measured at multiple points along the dam's crest during the water storage stage. As shown in Fig. 11 a, an increase in the inflow leads to a shorter seepage development time and simultaneously decreases the settlement rate. Additionally, as dam height increases, the dam volume increases, resulting in the rise in the settlement rate. An increase in the downstream slope angle leads to greater amplitude and likelihood of slope deformation, making steeper slopes more prone to instability (Jiang et al., 2020). Thus, dam settlement is more pronounced under steeper downstream slope angles. Moreover, as the uneven coefficient ( $d_{60}/d_{10}$ ) increases, the grain size distribution becomes more irregular, leading to an overall downward trend in the settlement rate.

Based on this analysis, the settlement rate of the dam is influenced by initial parameters such as upstream inflow rate, dam height, downstream slope angle, and soil particle size distribution. In this study, 34 sets of data were randomly selected to establish the relationship between the settlement rate  $k_{\rm h}$  and the upstream inflow rate  $Q_{\rm s}$ , dam height  $H_{\rm d}$ , uneven coefficient  $d_{\rm 60}/d_{\rm 10}$ , downstream slope angle  $\alpha$ , dam base width  $W_{\rm d}$ , and gravitational acceleration g:

$$k_{\rm h} = f(H_{\rm d}, Q_{\rm s}, d_{60}/d_{10}, \tan\alpha, W_{\rm d}, g)$$
 (9)

Using  $H_d$  and g as the basic dimensionless quantity to measure variables, we can obtain

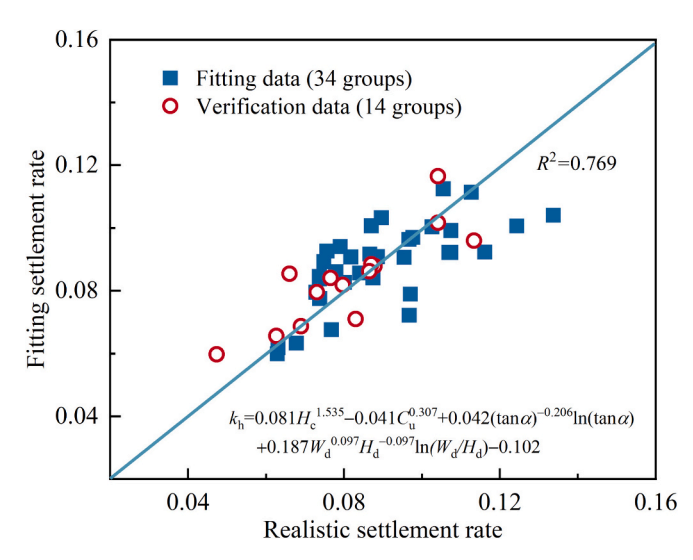


Fig. 12. Verification of prediction formula of settlement rate.

$$k_{\rm h} = f\left(\frac{H_{\rm d}}{\sqrt[5]{Q_{\rm s}^2/g}}, \frac{d_{60}}{d_{10}}, \tan\alpha, \frac{W_{\rm d}}{H_{\rm d}}\right) \tag{10}$$

Based on the data obtained, further fitting can be conducted to obtain  $(H_c = H_d/(Q_s^2/g)^{0.2})$ :

$$\begin{split} k_{\rm h} &= 0.081 H_{\rm c}^{0.307} - 0.042 C_{\rm u}^{0.206} + \frac{0.112 ln(tan\alpha)}{(tan\alpha)^{0.097}} + 0.187 \frac{{W_{\rm d}}^{0.097}}{H_{\rm d}^{0.097}} ln\bigg(\frac{W_{\rm d}}{H_{\rm d}}\bigg) \\ &- 0.102 \end{split} \tag{11}$$

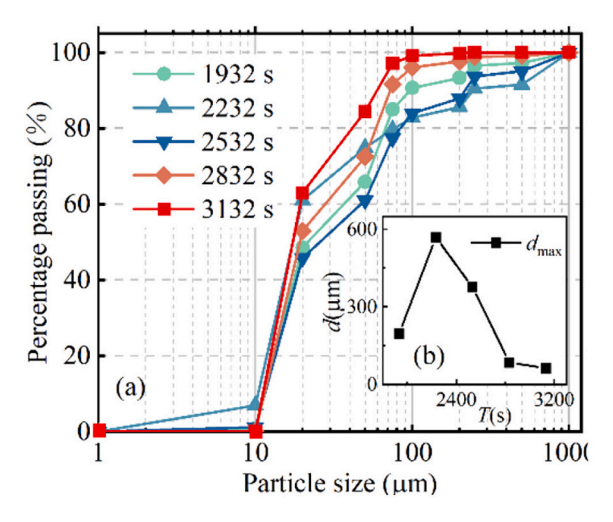
In this study, 14 random experimental data were used to validate the formula (Fig. 12). The  $R^2$  value was calculated to be 0.769.

## 3.4. Change in soil particles in dam

During the water storage stage, infiltration through seepage channels results in the continual removal of filling particles from the gaps within the soil skeleton. This loss of particles disrupts the internal stress distribution of the dam, ultimately leading to instability (Shi et al., 2022; Zhou et al., 2022a).

The observed variations in the particle size distribution during seepage flow indirectly reflect changes in the soil particle composition within the dominant seepage channel area (Chen et al., 2023). In the case of SA1 ( $Q_s = 0.35 \times 10^{-3} \text{ m}^3/\text{s}$ ,  $H_d = 30 \text{ cm}$ ,  $\alpha = 45^\circ$ , grain size distribution 6), the downstream seepage of the slope appears in T =1932 s. At T = 1932-3132 s, there is a significant presence of 10–20  $\mu$ m particles, accounting for more than 45 % of the total (Fig. 13 c). At T =1932 s, the maximum particle size in the seepage flow reaches 251  $\mu m$ . At T = 2832 s, sliding occurs on the downstream slope, leading to collapse and blockage within the seepage channel. As the water head increases, the size of soil particles transported by seepage typically grows, causing an increase in the maximum particle size. After T = 3132s, the seepage channel within the dam tends to stabilize temporarily before the seepage water pressure reaches a critical point, and the maximum particle size erosioned by the seepage remains relatively stable (Chang and Zhang, 2013; Sharif et al., 2015).

Based on Fig. 13 c, while the maximum experimental soil particle loss can reach 593  $\mu$ m, the predominant particle loss remains concentrated in the 10–75  $\mu$ m range. As a result, soil erosion due to seepage can be bifurcated into two components: erosion within the dam and erosion on the downstream slope surface (Bendahmane et al., 2008). Notably, the convergence of seepage flow on the downstream surface may lead to



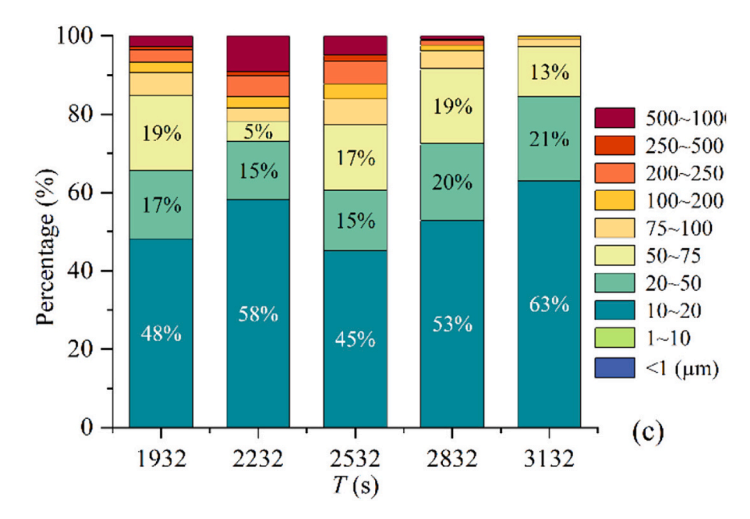
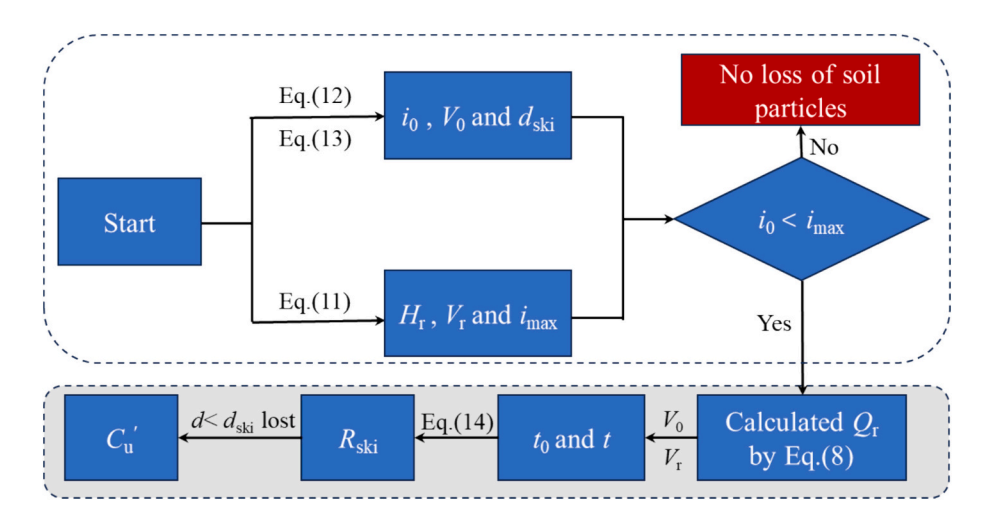


Fig. 13. Particle changes in seepage flow: (a) particle grain size distribution curve; (b) maximum size of particles from seepage flow; and (c) particle size distribution in seepage flow. The particle size of less than 90 % of the soil mass was considered the representative particle size of the seepage erosion particles in the experiment.



**Fig. 14.** The calculation process of particle size loss and soil non-uniformity coefficient in particle loss area. Given that the experimentally determined maximum particle size of loss is somewhat influenced by particle blockage phenomena, the  $d_{ski}$  was selected for the theoretical maximum particle size capable of being eroded by seepage. In the same time, we have assuming that particles below are proportionally lost by  $R_{ski}$ .

**Table 4** Variation in the soil particle distribution in the seepage area. The  $d_{\rm max}$  represents the maximum particle size of the downstream seepage flow, as measured in the experiment.

Condition	$d_{\max}(\mu m)$	$d_{\rm ski}(\mu { m m})$	$R_{ m ski}$	$C_{ m u}$	C'u	$C_{\rm u}/C'_{\rm u}$
SA1	790	124.77	0.028	20.31	23.42	1.15
DH4	1240	83.34	0.016	46.49	49.34	1.06
GS4	490	169.00	0.009	30.10	30.85	1.02
GS9	170	100.64	0.018	46.48	49.38	1.06

a maximum particle size significantly larger than the predominant particles.

For this result, it is reasonable to prioritize the principal particle size most susceptible to seepage erosion over the actual maximum particle size observed, as the latter represents a relatively small fraction. The loss of soil primarily occurs after the seepage channel has penetrated. The effective particle size formula proposed by Sha (1981) can be used to determine the penetration of the seepage channel:

$$i = \left(\frac{\gamma_{\rm s}}{\gamma_{\rm w}} - 1\right) (1 - n) \alpha_{\rm sp} d_3 / d_{\rm ski} \tag{12}$$

$$d_{\rm ski} = \sqrt{\frac{36Aa_{\rm s}k_{\rm s}(1-n)^2}{gn^3}} \tag{13}$$

Chen et al. (2021b) established a formula for the loss of latent erosion soil, which allows the calculation of the mass of soil loss less than the corresponding particle size at different times:

$$R_{\rm ski} = \frac{U_{\rm S}^{\rm t}}{U_0} = 1 - \exp\left[-0.015 \left(\frac{i}{i_0}\right) \left(\frac{t}{t_0}\right)^{1.51}\right] \tag{14}$$

Using Eq. (14), the loss of the soil in the area affected by seepage can be determined (Fig. 14).

Usually, in addition to conducting flume experiments, the  $d_{\rm max}$  value obtained from indoor seepage experiments can also be used to determine the soil particle size affected by seepage. Subsequently, after the alteration of the particle size distribution, the  $d'_{60}/d'_{10}$  ratio can be derived (Table 4).

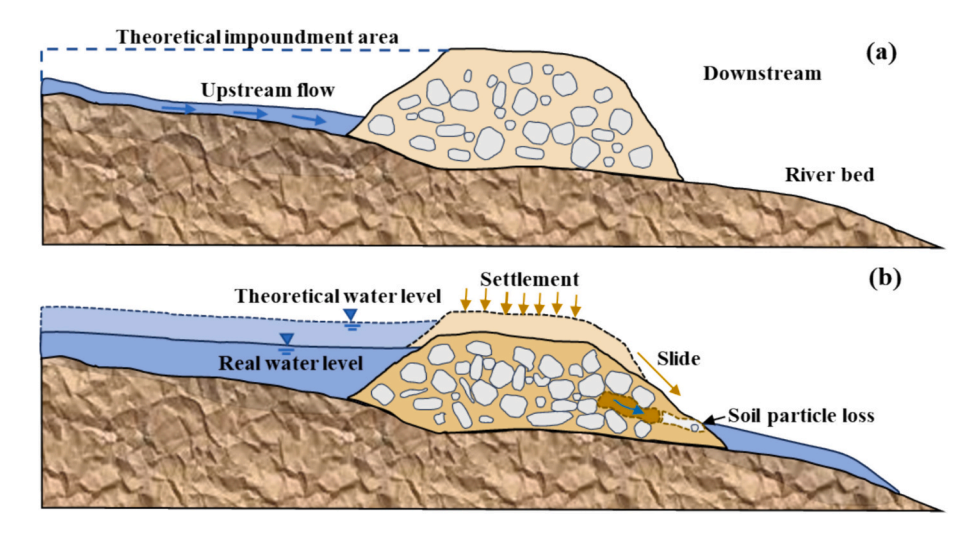


Fig. 15. The influence of seepage development on landslide dam characteristics: (a) initial landslide dam; and (b) changes in dam characteristics.

#### 4. Discussion

## 4.1. Influence of dam characteristic changes

In this study, the impact of seepage on dam characteristics is primarily reflected in the reduced rate of water level rise, deformation of the dam geometry, and the loss of soil particles, which lead to changes in dam stability (Fig. 15). The failure modes of landslide dams can be categorized into three types based on the failure characteristics: overtopping failure (62.5 %), seepage + overtopping failure (20.8 %), and seepage failure (4.16 %). The overtopping failure is more likely to occur in conditions characterized by large inflow and weak dam diversion capacity (Briaud et al., 2008; Tacconi et al., 2018). In such cases, effective seepage channels are typically not formed, and the impact of seepage is primarily evident in the changes to the dam's geometric shape. When upstream inflow is moderate and effective seepage channels can form, the dam is more prone to seepage + overtopping failure (Zhou et al., 2022b). The influence of seepage in these cases is reflected in reduced effective upstream inflow, alterations in dam geometry, and soil particle loss (Kalkani, 1997; Soueid Ahmed et al., 2020; Shafieiganjeh et al., 2024). When upstream inflow is low or the dam has a strong diversion capacity, seepage-induced particle loss becomes the dominant factor, leading to a higher probability of seepage failure. Furthermore, if the dam has a robust diversion capacity and a relatively coarse particle skeleton, the reduction in effective inflow may allow the dam to remain stable under flow erosion. In this study, such stable conditions were observed in about 12.5 % of cases.

For seepage + overtopping failure, the erosion process of soil particles can be divided into four stages: within the dam, internal erosion is primarily driven by seepage; above the seepage spill point, the exterior of the dam is mainly affected by overflow erosion; at the seepage spill point, erosion is influenced by both overflow and seepage; and below the seepage spill point, erosion is impacted by the combined flow of overflow and seepage. On the whole, erosion at the seepage spill point is representative of the overall erosion process in seepage + overtopping failure. The specific analysis process is as follows:

The theoretical seepage rate can be calculated using the calculation formula proposed by Shun (2016) for seepage in earth-rock dams:

$$\begin{cases} q = k_{\rm s} \frac{H_{\rm w}^2 - (H_2 + a_0)^2}{2[\Delta s + L - m_2(H_2 + a_0)]} & \text{upstream} \\ q = \frac{k_{\rm s} a_0}{m_2} \left( 1 + 2.3 lg \frac{H_2 + a_0}{a_0} \right) & \text{downstream} \end{cases}$$
(15)

In this study, the downstream water level  $H_2$  of the dam models was close to 2–4 mm, which was much smaller than the height of the dam. Therefore, a certain simplification can be made. Under the assumption that the seepage flow is consistent, the theoretical seepage flow can be obtained as follows:

$$q = k_{\rm s} \left[ \frac{\Delta s + L}{2m_2^2} + \sqrt{\frac{(\Delta s + L)^2}{4m_2^3} - \frac{H_{\rm w}^2}{m_2^2}} \right]$$
 (16)

The overflow formula (Singh and Snorrason, 1984) is used for this purpose:

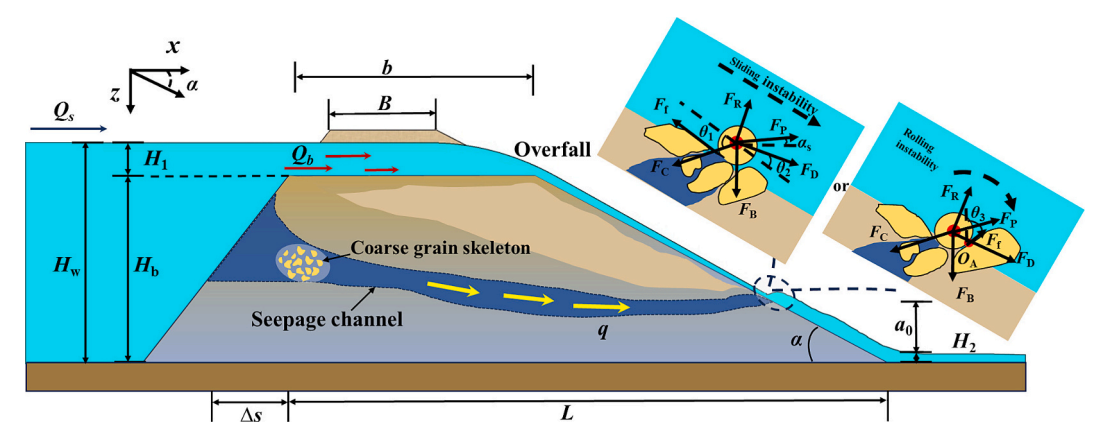


Fig. 16. Kinetics analysis of soil particle agglomeration on downstream dam slope. Sliding instability and rolling instability often occur randomly at the outlet.

$$Q_{\rm b} = k_{\rm sm} (c_1 b H_1^{1.5} + c_2 m_0 H_1^{1.5}) \tag{17}$$

In accordance with Eq.(16) and Eq.(17), it is evident that the changes in the dam height ( $H_d$ ) and upstream inflow rate ( $Q_s$ ) have a direct impact on the seepage (q) and overflow ( $Q_b$ ). Consequently, these changes subsequently influence the scouring capacity of the composite flow ( $Q_0$ ).

For the particle initiation process under the influence of composite flow, the solution can be obtained by referring to the following procedure. Under the assumption of uniform void ratio within the dam and spherical particles, the particles can experience several forces (Fig. 16): the drag force ( $F_D$ ) exerted by the water flow, the lifting force ( $F_R$ ) resulting from the flow velocity differences, the difference ( $F_B$ ) between the gravity and buoyancy of the particles, the seepage force ( $F_P$ ), and the friction ( $F_f$ ) between the soil particles and the slope surface (Shi et al., 2022). Furthermore, it was necessary to consider the bonding force ( $F_C$ ) between the eroded particles and the slope particles:

$$F_{\rm C} = \frac{\pi}{2} \varepsilon \left(\frac{\rho_0}{\rho_{\rm s}}\right)^{2.5} \rho_1 d \tag{18}$$

For the friction between the soil particles and the slope surface:

$$F_{\rm f} = f[F_{\rm B} cos\alpha + F_{\rm C} sin(\alpha + \theta_1) - F_{\rm R} cos\theta_2 - F_{\rm P} sin(\alpha - \alpha s) - F_{\rm D} sin\theta_2] \qquad \text{slide}$$
(19)

The particle instability process on the downstream slope can be specifically divided into sliding instability and rolling instability. For sliding instability, the force balance relationship can be established based on the particle center, and for rolling instability, the moment balance relationship can be established based on the particle-soil contact point  $O_A$ :

$$\begin{cases} F_{\rm D}cos\theta_2 + F_{\rm B}sin\alpha + F_{\rm C}cos(\alpha + \theta_1) - F_{\rm f} + F_{\rm P}cos(\alpha - \alpha s) - F_{\rm R}sin\theta_2 = 0 \text{ slide} \\ F_x sin\theta_3 \frac{d}{2} = F_z cos\theta_3 \frac{d}{2} \text{ roll} \end{cases}$$

Here:

$$\begin{cases} F_x = F_D cos(\alpha - \theta_2) + F_P cos(\alpha - \alpha s) + F_R sin(\alpha - \theta_2) - F_C cos\theta_1 \\ F_z = F_D sin(\alpha - \theta_2) + F_B - F_R cos(\alpha - \theta_2) + F_C sin\theta_1 + F_P sin(\alpha - \alpha s) \end{cases}$$

$$(21)$$

Based on Eq. (20) and Eq. (21), can obtain:

$$\begin{split} F_{\mathrm{D}}(\cos\theta_{2} - f\sin\theta_{2}) + F_{\mathrm{B}}(\sin\alpha - f\cos\alpha) + F_{\mathrm{C}}[\cos(\alpha + \theta_{1}) - f\sin(\alpha + \theta_{1})] \\ + F_{\mathrm{R}}(f\cos\theta_{2} - \sin\theta_{2}) + F_{\mathrm{P}}[\cos(\alpha - \alpha s) + f\sin(\alpha - \alpha s)] = \text{Oslide} \end{split}$$

$$F_{D}sin(\theta_{2} + \theta_{3} - \alpha) + F_{P}sin(\alpha s + \theta_{3} - \alpha) + F_{R}cos(\alpha - \theta_{2} - \theta_{3}) + F_{C}sin(\theta_{1} - \theta_{3}) - F_{R}cos\theta_{3} = 0 \quad \text{roll}$$
(23)

By combining the expressions of forces in the Section Abbreviations, it can be obtained:

$$u_{\mathrm{O}} = \begin{cases} \sqrt{\frac{4\left[\lambda_{1}gd^{2}(\rho_{\mathrm{s}} - \rho_{\mathrm{w}}) - \lambda_{2}\rho_{\mathrm{w}}gid^{2}(1+e) - 3\lambda_{3}\varepsilon\rho_{1}\right]}{3\rho_{1}d\left[(\cos\theta_{2} - f\sin\theta_{2})C_{\mathrm{D}} + (f\cos\theta_{2} - \sin\theta_{2})C_{\mathrm{L}}\right]}} & \mathrm{slide} \\ \sqrt{\frac{4\left[\lambda_{4}gd^{2}(\rho_{\mathrm{s}} - \rho_{\mathrm{w}}) - \lambda_{5}\rho_{\mathrm{w}}gid^{2}(1+e) + 3\lambda_{6}\varepsilon\rho_{1}\right]}{3\rho_{1}d\left[C_{\mathrm{D}}\sin(\theta_{2} + \theta_{3} - \alpha) + C_{\mathrm{L}}\cos(\alpha - \theta_{2} - \theta_{3})\right]}}} & \mathrm{roll} \end{cases}$$

The motion of soil particles is one of the microscopic manifestations of dam failure (Graf, 1984; Shen et al., 2022). Base on Eq.(24), it can be seen that the critical flow rate of the particle initiation is influenced by various factors. These include the properties of soil particles ( $\rho_s$  and f), the distribution characteristics of particles ( $\theta_1$ ,  $\theta_3$  and e), the geometric shape of the dam( $\alpha$ ), the upstream hydrological characteristics (i), and the flow intersection situation ( $\alpha_s$  and  $\theta_2$ ). The above analysis indirectly reflects the impact of changes in dam characteristics on the instability

**Table 5**Accuracy rate of model identification.

Predicted	Observed		Percent calibration (%)
	Stable dam	Unstable dam	
Stable	6.0	1.0	85.7
Unstable	2.0	39.0	95.1
Total percentage			93.7

**Table 6**Verification of case parameters.

	Zhou et a	al. (2022)	Ma et a	1. (2024)	Shi et al. (2017) and Zhang et al. (2015)		
	Case 1	Case 2	Case 3	Case 4	Case 5	Hongshiyan dam	
Q <sub>r</sub> (L/s)	49.34	48.89	6.26	6.26	6.26	127,219.20	
$H_{\rm r}({\rm m})$	1.66	1.85	0.20	0.22	0.22	81.35	
$k_{\rm s}(\times 10^{-5}$ m/s)	2.90	2.90	1.80	5.20	1.90	0.10	
$d'_{60}/d'_{10}$	20.32	26.10	4.20	19.26	20.26	26.10	
$tan\alpha$	0.81	0.81	0.50	0.50	0.50	0.27	
$W_{\rm d}({\rm m})$	10.00	5.50	1.20	1.20	1.20	1807.00	
$V_{\rm r}({\rm m}^3)$	500.00	500.00	0.24	0.24	0.24	260,000,000.00	
у	7.26	0.15	27.65	13.43	18.65	-0.86	
Dam stability	U	U	U	U	U	S	

and failure process of the dam.

## 4.2. Judgment of dam stability

(20)

The upstream inflow rate plays a crucial role in determining the rate of water level rise and the scouring capacity of the overflow. Previous studies (Dong et al., 2011b; Hu et al., 2011; Ruan et al., 2021b) have indicated that a smaller inflow and a larger storage capacity result in a longer seepage development time and a weaker scouring capacity of the overflow. The geometric conditions, such as the dam height ( $H_d$ ), downstream dam slope angle ( $\alpha$ ), and dam width ( $W_d$ ), also influence the development path of the seepage within the dam. Shang et al. (2003) and Stefanelli et al. (2018) indicated that a lower dam and a larger downstream slope angle lead to a shorter seepage path within the dam. Furthermore, the seepage coefficient of the soil particles significantly affects the rate of seepage development. Shen et al. (2020) and Meng

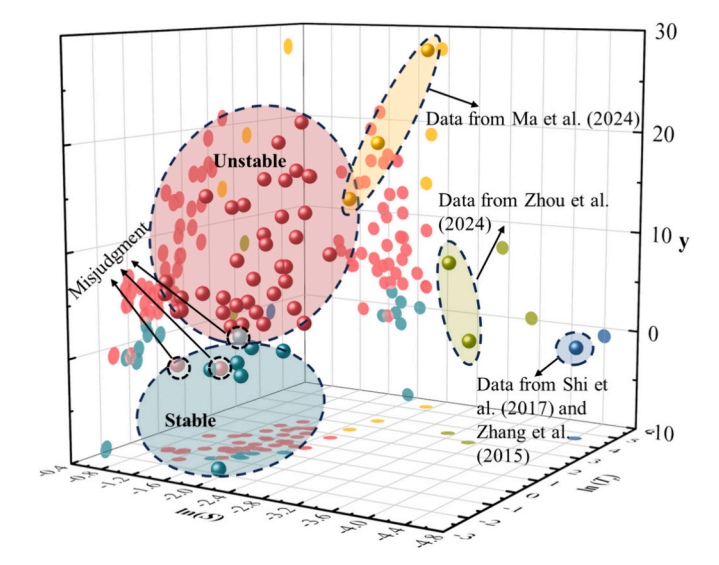


**Fig. 17.** Case distribution: y < 0 stable; y > 0 unstable.

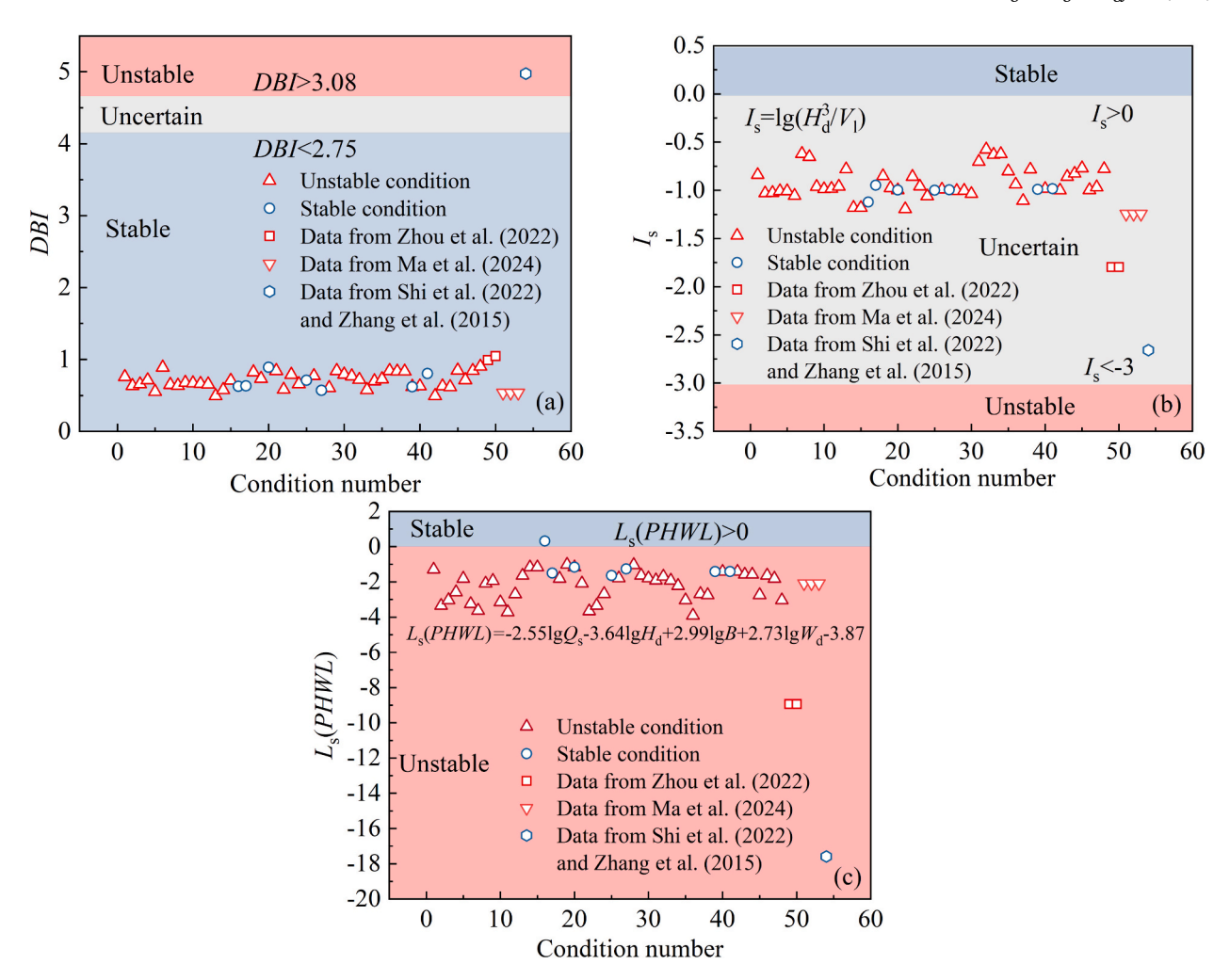


Fig. 18. The comparison of prediction model calculation result: (a) DBI model (Ermini and Casagli, 2003); (b) $I_s$  model (Korup, 2004); and (c)  $L_s(PHWL)$  model (Dong et al., 2011b).

et al. (2021) demonstrated that a higher seepage coefficient results in a greater seepage development rate.

Here, it can be assumed that the stability state of the dam is measured by y (dimensionless). Specifically, when y>0, the landslide dam will become unstable; when y<0, the dam maintains stability. Based on these findings and the exeperimental results, the landslide dam conforms to the following functional relationship:

$$y = f(Q_{\rm r}, d_{60}/d_{10}, k_{\rm s}, H_{\rm r}, \alpha, W_{\rm d}, V_{\rm r})$$
(25)

Using  $H_{\rm r}$  and  $k_{\rm s}$  as the basic dimensionless quantities to measure variables, we can obtain:

$$y = f\left(\frac{Q_{\rm r}}{H_{\rm r}^2 k_{\rm s}}, \frac{d_{60}'}{d_{10}'}, \tan\alpha, \frac{W_{\rm d}}{H_{\rm r}}, \frac{V_{\rm r}}{H_{\rm r}^3}\right)$$
 (26)

where  $H_r = (1-k_h)H_d$  and  $Q_r = (1-k_r)Q_s$ , which can be calculated using Eq.(8) and Eq.(11).

In reference to previous studies (Costa and Schuster, 1991; Cui et al., 2009; Dong et al., 2011b), let  $S = W_{\rm d}H_{\rm r}^2(\tan\alpha)/V_{\rm r}$  and  $T_{\rm r} = Q_{\rm r}/(H_{\rm r}^2k_{\rm s}C_{\rm u})$ . The experimental data consisting of 48 cases were randomly divided into a training set (21 unstable groups, three stable groups) and a target set (21 unstable groups, three stable groups) (Dong et al., 2011a). Using parameters S and  $T_{\rm r}$ , a binary logistic regression model for dam stability was established. The model's predictive ability was tested using the confusion matrix presented in Tables 5 and 6:

$$y = 11.283ln(S) + 5.913ln(T_r) + 22.175$$
(27)

If y < 0, the dam is stable; otherwise, the dam is considered unstable. By comparing Tables 5 and 6 with Fig. 17, the applicability of the formula was verified through six cases. In the same time, this formula has a higher reliability under existing boundary condition by comparing with other three existing formulas (Fig. 18). This result may be related to factors such as the scale of the data and the parameters considered in the formula. In addition, the greater the absolute value of y, the higher the probability of stability or instability of the corresponding landslide dam (Dong et al., 2011a).

## 4.3. Limitation

Due to the sudden nature of landslide dam formation, detailed records of dam parameters are often unavailable in many cases. As a result, in the verification phase of this study, this study supplemented the data by selecting landslide dams of the similar type and utilizing data from relevant literature. However, the data used for verification may still differ from the actual parameters of natural cases.

The accuracy of logistic regression models is highly dependent on the choice of the database. Although the similarity between the model dams and prototype dams was verified using certain dimensionless coefficients, significant scale differences between the two still objectively exist. Therefore, the logistic regression model developed in this study serves more as a reference for identifying dam stability under field conditions.

#### 5. Conclusion

Through the analysis of 48 experimental groups, we examined the dynamic alterations in dam characteristics under seepage and their impact on dam stability. The following conclusions were drawn:

- (1) Seepage not only effectively slows down the rate of water level rise but also induces changes in the internal stress distribution of the dam, leading to increased non-uniformity in the structure of noncohesive landslide dams. Additionally, a lag feedback loop between dam deformation and seepage develop was evidenced by the time discrepancy in pore pressure fluctuations corresponding to the progression of the breach.
- (2) Although the maximum diversion rate reached 74.7 % through water infiltration and downstream slope outflow in this study, a certain upper limit to the diversion capacity is determined by the dam's external geometric shape and material composition. The deformation of the dam, manifested as settlement and downstream slope sliding, exhibits non-uniform distribution both temporally and spatially, which correlates with the non-uniform development of seepage within the dam. To further evaluate the impact of seepage development on dam characteristics, two dimensionless evaluation models, based on initial inflow conditions, geometric conditions, and particle distribution parameters, were developed and demonstrated to fit the experimental data.
- (3) The erosion process caused by seepage during the water storage stage can be divided into two forms: internal erosion within the dam and downstream slope erosion. As particles are continuously lost, the soil structure within the dam becomes more complex and unevenly reinforced. In this study, the non-uniformity coefficient of the soil in the seepage channel area increased by 1.02 to 1.15 times under the influence of seepage before dam failure.
- (4) Based on the theoretical analysis of seepage and overtopping failure, it has been verified that the stability of the dam under flow erosion is influenced by water flow conditions, dam geometry, and soil materials. Considering the reduction in effective inflow, dam settlement, and the loss of soil particles caused by seepage within the dam, it can be assumed that the stability of the dam does not follow a straightforward trend of becoming either more stable or more unstable as seepage progresses; instead, it

- exhibits a complex response that may vary depending on the specific conditions.
- (5) To quickly assess dam stability, a binary logistic regression model was developed based on the dam characteristics change. The model incorporates composite variables S and  $T_{\rm r}$ , as follows:  $y=11.283\ln(S)+5.913\ln(T_{\rm r})+22.157$  (y>0 unstable; y<0 stable). Six cases from a previous study were used to validate this model, showing that the predicted stability aligned with actual results. This indicates that this model can give a certain reference for the identification of dam stability.

#### CRediT authorship contribution statement

Xiao Li: Conceptualization, Supervision, Writing – review & editing. Huayong Chen: Data curation, Methodology, Writing – original draft. Xiaoqing Chen: Formal analysis, Funding acquisition. Tao Wang: Data curation, Visualization. Yao Jiang: Validation, Investigation. Hechun Ruan: Validation, Investigation.

#### **Declaration of competing interest**

The authors declare that they have no known competing financial interests or personal relationships that could have appeared to influence the work reported in this paper.

#### Data availability

Data will be made available on request.

#### Acknowledgement

Financially supported by the National Natural Science Foundation of China (Grant No. U20A20112 , U21A2008), Science and Technology Program of Tibet Autonomous Region, China (Grant No. XZ202201ZY0011G), CAS Light of West China Program and Science and Technology Research Program of Institute of Mountain Hazards and Environment, Chinese Academy of Sciences (IMHE-ZDRW-02). The authors thank the support from the Dongchuan Debris Flow Observation and Research Station (DDFORS), Chinese Academy of Sciences.

Appendix A

Table A1

Database of fitted.

Working condition	$H_{\rm d}/(Q_{\rm s}^2/g)^{1/5}$	$d_{60}/d_{10}$	$\tan \alpha$	$W_{\rm d}/H_{\rm d}$	S	$T_{\rm r}$	$k_{\rm r}$		$k_{ m h}$		у
							Observed	Calculated	Observed	Calculated	
UI1	20.648	46.487	0.869	3.080	0.455	0.394	0.743	0.645	0.104	0.137	-0.842
UI2	5.178	46.487	0.466	4.242	6.001	0.124	0.311	0.373	0.063	0.047	12.248
UI3	6.667	46.487	0.466	4.242	3.752	0.090	0.518	0.427	0.068	0.052	10.050
UI4	6.504	46.487	0.466	4.242	2.685	0.091	0.416	0.484	0.069	0.060	7.425
UI5	7.655	46.487	0.466	4.242	1.216	0.124	0.453	0.548	0.073	0.073	2.379
UI6	6.933	20.315	0.700	3.525	5.715	0.177	0.513	0.463	0.077	0.089	15.625
UI7	9.426	46.487	0.466	3.975	1.586	0.278	0.474	0.547	0.063	0.061	14.017
UI8	16.687	46.487	0.466	3.975	0.305	0.292	0.570	0.607	0.089	0.091	3.790
UI9	13.214	46.487	0.577	3.829	0.926	0.144	0.747	0.571	0.080	0.084	4.372
UI10	6.350	46.487	0.577	3.829	3.536	0.158	0.418	0.450	0.063	0.064	11.961
UI11	4.839	46.487	0.577	3.829	7.493	0.251	0.23`0	0.345	0.047	0.055	16.193
UI12	8.993	46.487	0.577	3.829	2.111	0.138	0.672	0.507	0.083	0.071	9.497
DH1	19.621	46.487	0.466	4.019	0.371	0.293	0.564	0.608	0.113	0.107	4.820
DH2	8.759	46.487	0.466	4.575	1.553	0.046	0.639	0.477	0.088	0.072	2.326
DH3	11.455	46.487	0.466	4.375	0.853	0.079	0.676	0.477	0.066	0.072	2.305
DH4	17.027	46.487	0.466	4.146	0.421	0.138	0.585	0.536	0.087	0.076	-0.044

(continued on next page)

#### Table A1 (continued)

Working condition	$H_{\rm d}/(Q_{\rm s}^2/g)^{1/5}$	$d_{60}/d_{10}$	tan $\alpha$	$W_{ m d}/H_{ m d}$	S	S T <sub>r</sub>	$k_{\rm r}$		$k_{ m h}$		у
							Observed	Calculated	Observed	Calculated	
DH5	18.390	46.487	0.700	3.358	1.101	0.339	0.613	0.587	0.097	0.085	-0.903
DH6	15.779	46.487	0.700	3.525	0.376	0.093	0.651	0.630	0.134	0.132	8.098
DH7	16.866	53.091	0.999	3.097	0.227	0.134	0.680	0.627	0.105	0.115	-1.332
DH8	4.772	46.487	0.466	4.575	5.366	0.075	0.350	0.639	0.074	0.159	-1.381
DH9	8.357	46.487	0.466	4.575	1.688	0.044	0.530	0.340	0.087	0.057	8.384
DH10	6.725	30.107	0.700	3.430	8.675	0.144	0.485	0.478	0.097	0.080	13.123
DH11	9.204	20.315	0.700	3.430	4.277	0.240	0.580	0.518	0.080	0.092	15.323
DH12	6.734	20.315	0.700	3.658	7.828	0.066	0.647	0.455	0.116	0.094	15.670

**Table B1**Database of fitted (continued).

Working condition	$H_{\rm d}/(Q_{\rm s}^2/g)^{1/5}$	$d_{60}/d_{10}$	tan α	$W_{\rm d}/H_{\rm d}$	S	$T_{\rm r}$	$k_{\rm r}$		$k_{ m h}$		у
							Observed	Calculated	Observed	Calculated	
SA1	13.520	29.852	0.700	3.525	0.725	0.159	0.680	0.605	0.103	0.116	1.353
SA2	12.462	29.852	0.999	3.097	0.484	0.188	0.700	0.617	0.113	0.133	3.519
SA3	12.418	46.487	0.364	4.845	0.149	0.107	0.613	0.530	0.086	0.068	-9.781
SA4	15.533	46.487	0.268	5.563	0.373	0.220	0.523	0.464	0.107	0.057	3.667
SA5	15.811	46.487	0.364	4.578	0.347	0.253	0.560	0.605	0.076	0.103	2.381
SA6	15.715	46.487	0.577	3.562	0.327	0.309	0.595	0.617	0.087	0.125	4.109
SA7	13.673	46.487	0.268	5.830	1.483	0.094	0.686	0.634	0.095	0.124	6.392
SA8	14.423	46.487	0.700	3.525	0.702	0.118	0.610	0.508	0.107	0.068	4.950
SA9	14.561	46.487	0.999	3.097	0.536	0.215	0.696	0.572	0.090	0.080	3.841
SA10	20.648	46.487	0.869	3.080	0.295	0.412	0.743	0.624	0.104	0.101	5.362
SA11	15.240	20.315	0.700	3.303	1.599	0.674	0.715	0.600	0.082	0.100	5.269
SA12	6.116	12.313	0.700	3.430	5.545	0.122	0.443	0.441	0.074	0.089	20.757
SA13	6.511	30.107	0.700	3.658	0.638	0.298	0.554	0.455	0.084	0.087	7.406
GS1	18.510	28.804	0.466	4.075	2.345	0.245	0.600	0.554	0.124	0.090	15.465
GS2	14.346	46.487	0.466	4.242	0.627	0.123	0.581	0.568	0.078	0.080	0.354
GS3	10.423	20.315	0.466	4.242	1.798	0.066	0.556	0.569	0.087	0.095	5.021
GS4	10.277	30.107	0.466	4.242	0.499	0.199	0.550	0.568	0.079	0.088	-2.032
GS5	12.008	50.275	0.466	4.242	1.979	0.157	0.569	0.568	0.074	0.102	6.092
GS6	11.657	53.091	0.466	4.075	3.843	0.195	0.595	0.599	0.077	0.113	6.393
GS7	9.926	28.804	0.466	4.075	7.679	0.180	0.527	0.599	0.097	0.123	10.373
GS8	20.107	53.091	0.466	4.075	1.225	0.272	0.620	0.554	0.075	0.100	18.878
GS9	10.609	46.487	0.700	3.525	0.645	0.147	0.526	0.605	0.107	0.103	2.262
GS10	11.720	46.487	0.466	4.242	0.989	0.125	0.652	0.548	0.073	0.073	3.442
GS11	15.730	30.107	0.700	3.303	0.823	0.192	0.708	0.600	0.087	0.107	12.928

#### References

- Bendahmane, F., Marot, D., Alexis, A., 2008. Experimental Parametric Study of Suffusion and Backward Erosion. J. Geotech. Geoenviron. Eng. 134, 57–67. https://doi.org/ 10.1061/(ASCE)1090-0241(2008)134:1(57).
- Briaud, J.L., Chen, H.C., Govindasamy, A., Storesund, R., 2008. Levee erosion by overtopping in New Orleans during the Katrina Hurricane. J. Geotech. Geoenviron. Eng. 134, 618–632. https://doi.org/10.1061/(ASCE)1090-0241(2008)134:5(618).
- Canuti, P., Casagli, N., Ermini, L., 1998. Inventory of landslide dams in the Northern Apennine as a model for induced flood hazard forecasting. In: Managing Hydro-Geological Disasters in a Vulnerable Environment. CNR-GNDCI and UNESCO IHP, Perugia, pp. 189–202.
- Casagli, N., Ermini, L., 1999. Geomorphic analysis of landslide dams in the Northern Apennine. Trans. Jpn. Geomorphol. 20, 219–249.
- Chang, D.S., Zhang, L.M., 2013. Critical hydraulic gradients of internal erosion under complex stress states. J. Geotech. Geoenviron. Eng. 139, 1454–1467. https://doi. org/10.1061/(ASCE)GT.1943-5606.0000871.
- Chen, S.C., Lin, T.W., Chen, C.Y., 2015. Modeling of natural dam failure modes and downstream riverbed morphological changes with different dam materials in a flume test. Eng. Geol. 188, 148–158. https://doi.org/10.1016/j.enggeo.2015.01.016.
- Chen, K., Chen, T., Chen, X., Chen, H., Zhao, W., 2021a. An experimental determination of the relationship between the minimum height of landslide dams and the run-out distance of landslides. Landslides 18, 2111–2124. https://doi.org/10.1007/s10346-020-01605-1.
- Chen, Y., Wen, X., Xia, C., Long, H., 2021b. Latent erosion evolution characteristics and prediction model of silty sand under seepage action. J. Civil Environ. Eng. 1–9.
- Chen, C., Wang, Y., Zhang, J., Zhang, H., Li, H., Chen, Q., 2023. A preliminary study of landslide dam failures induced by the combined influence of piping and overtopping. J. Hydrol. 625, 129984 https://doi.org/10.1016/j.jhydrol.2023.129984.
- Costa, J.E., Schuster, R.L., 1988. The formation and failure of natural dams. Geol. Soc. Am. Bull. 100, 1054–1068. https://doi.org/10.1130/0016-7606(1988)1002.3.CO;2.

- Costa, J.E., Schuster, R.L., 1991. Documented historical landslide dams from around the world. In: US Geological Survey Report 2331-1258. https://doi.org/10.3133/ ofr91239.
- Cui, P., Zhu, Y., Han, Y., Chen, X., Zhuang, J., 2009. The 12 May Wenchuan earthquake-induced landslide lakes: distribution and preliminary risk evaluation. Landslides 6, 209–223. https://doi.org/10.1007/s10346-009-0160-9.
- Dong, J.J., Li, Y.S., Kuo, C.Y., Sung, R.T., Li, M.H., Lee, C.T., Chen, C.C., Lee, W.R., 2011a. The formation and breach of a short-lived landslide dam at Hsiaolin village, Taiwan—part I: post-event reconstruction of dam geometry. Eng. Geol. 123, 40–59. https://doi.org/10.1016/j.enggeo.2011.04.001.
- Dong, J.J., Tung, Y., Chen, C., Liao, J., Pan, Y., 2011b. Logistic regression model for predicting the failure probability of a landslide dam. Eng. Geol. 117, 52–61. https:// doi.org/10.1016/j.enggeo.2010.10.004.
- Ermini, L., Casagli, N., 2003. Prediction of the behaviour of landslide dams using a geomorphological dimensionless index. Earth Surf. Proc. Landforms: J. British Geomorphol. Res. Group. 28, 31–47.
- Graf, W.H., 1984. Hydraulics of Sediment Transport. Water Resources Publications, Colorado, p. 513.
- Hu, X., Luo, G., Lv, X., Huang, R., Shi, Y., 2011. Analysis on dam-breaking mode of Tangjiashan barrier dam in Beichuan county. J. Mt. Sci. 8, 354–362. https://doi.org/ 10.1007/s11629-011-2097-4.
- Jiang, X., Wei, Y., Wu, L., Hu, K., Zhu, Z., Zou, Z., Xiao, W., 2019. Laboratory experiments on failure characteristics of non-cohesive sediment natural dam in progressive failure mode. Environ. Earth Sci. 78, 1–14. https://doi.org/10.1007/ s12665-019-8544-1.
- Jiang, X., Wörman, A., Chen, P., Huang, Q., Chen, H., 2020. Mechanism of the progressive failure of non-cohesive natural dam slopes. Geomorphology 363, 107198. https://doi.org/10.1016/j.geomorph.2020.107198.
- Kalkani, E.C., 1997. Geological conditions, seepage grouting, and evaluation of piezometer measurements in the abutments of an earth dam. Eng. Geol. 46, 93–104. https://doi.org/10.1016/S0013-7952(96)00101-9.

- Korup, O., 2004. Geomorphometric characteristics of New Zealand landslide dams. Eng. Geol. 73, 13–35. https://doi.org/10.1016/j.enggeo.2003.11.003.
- Li, D.Y., Zheng, D.F., Wu, H., Shen, Y.Q., Nian, T.K., 2021. Numerical simulation on the longitudinal breach process of landslide dams using an improved coupled DEM-CFD method. Front. Earth Sci. 9 https://doi.org/10.3389/feart.2021.673249.
- Liao, H.M., Yang, X.G., Lu, G.D., Tao, J., Zhou, J.W., 2022. A geotechnical index for landslide dam stability assessment. Geomat. Nat. Haz. Risk 13, 854–876. https://doi. org/10.1080/19475705.2022.2048906.
- Liu, Z., Chen, Q., Li, X., Chen, C., Zhou, C., Wang, C., 2023. A review of the research on the failure potential of landslide dams caused by overtopping and seepage. Nat. Hazards 116, 1513–1538. https://doi.org/10.1007/s11069-022-05726-9.
- Ma, C., Peng, M., Zhang, L., Shi, Z., Zhou, J., Chen, H., Zhu, Y., Li, Z., 2024. Erosion, deposition and breach evolution of landslide dams composed of various dam material types based on flume tests. Eng. Geol. 107598 https://doi.org/10.1016/j.enggeo.2024.107598.
- Macchione, F., Graziano, A.A., 2024. Dimensionless attenuation of dam-breach flood wave propagating along a river. J. Hydrol. 641, 131765 https://doi.org/10.1016/j. ihydrol.2024.131765.
- Meng, C.K., Chen, K.T., Niu, Z.P., Di, B.F., Ye, Y.J., 2021. Influence of Internal Structure on breaking Process of Short-Lived Landslide Dams. Front. Earth Sci. 9 https://doi. org/10.3389/feart.2021.604635.
- Ming, P., Lu, J., Cai, X., Liu, M., Hu, S., 2022. Experimental study on internal erosion and seepage in the foundation of a dike under variable water head. Eur. J. Environ. Civ. Eng. 26, 5073–5087. https://doi.org/10.1080/19648189.2021.1883118.
- Nardini, O., Confuorto, P., Intrieri, E., Montalti, R., Montanaro, T., Robles, J.G., Poggi, F., Raspini, F., 2024. Integration of satellite SAR and optical acquisitions for the characterization of the Lake Sarez landslides in Tajikistan. Landslides 21, 1385–1401. https://doi.org/10.1007/s10346-024-02214-v.
- Nian, T., Wu, H., Li, D.Y., Zhao, W., Takara, K., Zheng, D., 2020. Experimental investigation on the formation process of landslide dams and a criterion of river blockage. Landslides 17, 2547–2562. https://doi.org/10.1007/s10346-020-01494-
- Peng, M., Zhang, L., 2012. Breaching parameters of landslide dams. Landslides 9, 13–31. https://doi.org/10.1007/s10346-011-0271-y.
- Peng, M., Ma, C.Y., Chen, H.X., Zhang, P., Zhang, L.M., Jiang, M.Z., Zhang, Q.Z., Shi, Z. M., 2021. Experimental study on breaching mechanisms of landslide dams composed of different materials under surge waves. Eng. Geol. 291, 106242 https://doi.org/10.1016/j.engepc.2021.106242.
- Ruan, H., Chen, H., Li, Y., Chen, J., Li, H., 2021a. Study on the downcutting rate of a debris flow dam based on grain-size distribution. Geomorphology 391, 107891. https://doi.org/10.1016/j.geomorph.2021.107891.
- Ruan, H., Chen, H., Wang, T., Chen, J., Li, H., 2021b. Modeling Flood Peak Discharge Caused by Overtopping failure of a Landslide Dam. Water 13, 921. https://doi.org/ 10.3390/w13070921.
- Sha, J., 1981. Study on Piping in Porous Media. Hydro-Science and Engineering, pp. 89–93 (Chinese).
- Shafieiganjeh, R., Schneider-Muntau, B., Ostermann, M., Gems, B., 2024. Seepage process understanding at long-existing landslide dams through numerical analysis and hydrological measurements. Eng. Geol. 335, 107524 https://doi.org/10.1016/j.engep. 2024 107524
- Shang, Y., Yang, Z., Li, L., Liao, Q., Wang, Y., 2003. A super-large landslide in Tibet in 2000: background, occurrence, disaster, and origin. Geomorphology 54, 225–243. https://doi.org/10.1016/S0169-555X(02)00358-6
- Sharif, Y.A., Elkholy, M., Hanif Chaudhry, M., Imran, J., 2015. Experimental study on the piping erosion process in earthen embankments. J. Hydraul. Eng. 141, 04015012. https://doi.org/10.1061/(ASCE)HY.1943-7900.0001019.
- Shen, D.Y., 2022. Study on Rapid and Quantitative Hazard Assessment Method of Landslide Dams. Tongji University (Chinese).
- Shen, D.Y., Shi, Z., Peng, M., Zhang, L., Jiang, M., 2020. Longevity analysis of landslide dams. Landslides 17, 1797–1821. https://doi.org/10.1007/s10346-020-01386-7.
- Shen, D.Y., Shi, Z., Zheng, H., Yang, J., Hanley, K.J., 2022. Effects of grain composition on the stability, breach process, and breach parameters of landslide dams. Geomorphology 413, 108362. https://doi.org/10.1016/j.geomorph.2022.108362.

- Shen, D., Shi, Z., Yang, J., Zheng, H., Zhu, F., 2024. Qualitative analysis of the overtopping-induced failure of noncohesive landslide dams: effect of material composition and dam structure on breach mechanisms. J. Hydrol. 638, 131580 https://doi.org/10.1016/j.jhydrol.2024.131580.
- Shi, Z.M., Wang, Y.Q., Peng, M., Chen, J.F., Yuan, J., 2015. Characteristics of the landslide dams induced by the 2008 Wenchuan earthquake and dynamic behavior analysis using large-scale shaking table tests. Eng. Geol. 194, 25–37. https://doi.org/ 10.1016/j.enggeo.2014.10.009.
- Shi, Z.M., Xiong, X., Peng, M., Zhang, L.M., Xiong, Y.F., Chen, H.X., Zhu, Y., 2017. Risk assessment and mitigation for the Hongshiyan landslide dam triggered by the 2014 Ludian earthquake in Yunnan, China. Landslides 14, 269–285. https://doi.org/ 10.1007/s10346-016-0699-1.
- Shi, Z.M., Zhang, G., Peng, M., Zhang, Q., Zhou, Y., Zhou, M., 2022. Experimental investigation on the breaching process of landslide dams with differing materials under different inflow conditions. Materials 15, 2029. https://doi.org/10.3390/ ma15062029
- Shrestha, B.B., Nakagawa, H., 2016. Hazard assessment of the formation and failure of the Sunkoshi landslide dam in Nepal. Nat. Hazards 82, 2029–2049. https://doi.org/ 10.1007/s11069-016-2283-3.
- Shun, D., 2016. Shuilixue, two ed. Zhenzhou(Chinese).
- Singh, K.P., Snorrason, A., 1984. Sensitivity of outflow peaks and flood stages to the selection of dam breach parameters and simulation models. J. Hydrol. 68, 295–310. https://doi.org/10.1016/0022-1694(84)90217-8.
- Soueid Ahmed, A., Revil, A., Bolève, A., Steck, B., Vergniault, C., Courivaud, J.R., Jougnot, D., Abbas, M., 2020. Determination of the permeability of seepage flow paths in dams from self-potential measurements. Eng. Geol. 268, 105514 https://doi. org/10.1016/j.enggeo.2020.105514.
- Stefanelli, C.T., Segoni, S., Casagli, N., Catani, F., 2016. Geomorphic indexing of landslide dams evolution. Eng. Geol. 208, 1–10. https://doi.org/10.1016/j. enggeo.2016.04.024.
- Stefanelli, C.T., Vilímek, V., Emmer, A., Catani, F., 2018. Morphological analysis and features of the landslide dams in the Cordillera Blanca. Peru. Landslides 15, 507–521. https://doi.org/10.1007/s10346-017-0888-6.
- Swanson, F.J., Oyagi, N., Tominaga, M., 1986. Landslide Dams in Japan, Landslide Dams: Processes, Risk, and Mitigation. ASCE, Reston, VA, pp. 131–145.
- Tacconi, S.C., Vilímek, V., Emmer, A., Catani, F., 2018. Morphological analysis and features of the landslide dams in the Cordillera Blanca, Peru. Landslides 15, 507–521. https://doi.org/10.1007/s10346-017-0888-6.
- Zhang, S., Xie, X., Wei, F., Chernomorets, S., Petrakov, D., Pavlova, I., Tellez, R.D., 2015. A seismically triggered landslide dam in Honshiyan, Yunnan, China: from emergency management to hydropower potential. Landslides 12, 1147–1157. https://doi.org/10.1007/s10346-015-0639-5.
- Zhang, Q., Chen, Z., Li, Y., Yu, S., Wang, L., Zhou, X., Wu, S., 2023. Quantitative assessment on landslide dam risks and mitigation: an in-depth study on the Baige lake breach. Environ. Earth Sci. 82, 1–20. https://doi.org/10.1007/s12665-023-10778-6
- Zheng, H., Shi, Z., Shen, D., Peng, M., Hanley, K.J., Ma, C., Zhang, L., 2021. Recent advances in stability and failure mechanisms of landslide dams. Front. Earth Sci. 9, 201. https://doi.org/10.3389/feart.2021.659935.
- Zheng, Y., Hu, W., van Asch, T., Li, Y., Fan, Y., 2024. Experimental study on the failure mechanisms of non-cohesive soil landslide dams with different scales. Eng. Geol. 333, 107489 https://doi.org/10.1016/j.enggeo.2024.107489.
- Zhong, Q., Wang, L., Chen, S., Chen, Z., Liu, J., 2021. Breaches of embankment and landslide dams - State of the art review. Earth Sci. Rev. 103597 https://doi.org/ 10.1016/j.earscirev.2021.103597.
- Zhou, G.G., Li, S., Lu, X., Tang, H., 2022a. Large-scale landslide dam breach experiments: Overtopping and "overtopping and seepage" failures. Eng. Geol. 304, 106680 https://doi.org/10.1016/j.enggeo.2022.106680.
- Zhou, G.G., Lu, X., Xie, Y., Cui, K.F.E., Tang, H., 2022b. Mechanisms of the non-uniform breach morphology evolution of landslide dams composed of unconsolidated sediments during overtopping failure. J. Geophys. Res. Earth 127, e2022JF006664. https://doi.org/10.1029/2022JF006664.